Recognition Dynamics Up to Microseconds Revealed from an RDC-Derived Ubiquitin Ensemble in Solution

Oliver F. Lange, ¹* Nils-Alexander Lakomek, ²* Christophe Farès, ² Gunnar F. Schröder, ¹ Korvin F. A. Walter, ² Stefan Becker, ² Jens Meiler, ³ Helmut Grubmüller, ¹ Christian Griesinger, ²† Bert L. de Groot ¹†

Protein dynamics are essential for protein function, and yet it has been challenging to access the underlying atomic motions in solution on nanosecond-to-microsecond time scales. We present a structural ensemble of ubiquitin, refined against residual dipolar couplings (RDCs), comprising solution dynamics up to microseconds. The ensemble covers the complete structural heterogeneity observed in 46 ubiquitin crystal structures, most of which are complexes with other proteins. Conformational selection, rather than induced-fit motion, thus suffices to explain the molecular recognition dynamics of ubiquitin. Marked correlations are seen between the flexibility of the ensemble and contacts formed in ubiquitin complexes. A large part of the solution dynamics is concentrated in one concerted mode, which accounts for most of ubiquitin's molecular recognition heterogeneity and ensures a low entropic complex formation cost.

rotein function relies on structural protein dynamics, with time scales ranging from picoseconds to beyond seconds. For molecular recognition, for example, proteins adapt their structure to different binding partners, often exhibiting large structural heterogeneity. In the past 30 years, atomic information on many dynamical processes has been accumulated from a broad variety of techniques (1, 2). Nuclear magnetic resonance (NMR) relaxation has been used to quantitatively probe protein dynamics at the fast end (picoseconds to nanoseconds) as well as in a much slower range (microseconds to milliseconds) of this broad spectrum of time scales (3-6). Relaxation of nuclear magnetization is caused by fluctuations of magnetic interactions between nuclei resulting from the nanosecond rotational tumbling of the molecule and internal dynamics. The amplitudes of these motions are expressed as so-called Lipari-Szabo order parameters S_{LS}^2 (7). Internal dynamics slower than the rotational tumbling time τ_c have no impact on the overall fluctuation of the magnetic interactions. Therefore, S_{LS}^2 order parameters reflect only sub- τ_c motions, at the fast end of time scales.

The slow range of time scales is accessible by relaxation dispersion measurements, based on the stochastic fluctuations of isotropic chemical shifts, which are independent of rotational tumbling (3, 5). Conformational heterogeneity

slower than 10 ms can be directly observed as peak splitting in NMR spectra. For backbone amides, motions faster than 50 µs do not result in sufficient line broadening to be detectable for relaxation dispersion measurements. These mea-

surements therefore probe motions slower than about 50 µs up to about 10 ms and have been used to characterize major structural changes and enzymatic reactions (6, 8). Except for certain favorable cases (9), it is, however, difficult to translate these fluctuations into ensembles of structures. Therefore, relaxation-based ensembles of solution structures take only motions faster than τ_c into account: They are limited to sub- τ_c dynamics (10, 11). These sub- τ_c motions are typically much smaller than the structural changes involved in molecular recognition and are likely to contribute mainly to the entropy of proteins (12-14). As a consequence, the structural heterogeneity observed in protein complexes has frequently been assumed to be inaccessible to equilibrium fluctuations in solution, thus favoring induced-fit models (15, 16).

RDCs probe supra- τ_c dynamics. RDCs are sensitive to motion from picoseconds to milliseconds, which includes the previously invisible time window between τ_c and 50 μ s, which we will call supra- τ_c . Indeed, RDCs recorded for ubiquitin, as well as for the B1 domain of protein G, hint at substantial dynamics between nanoseconds and microseconds (17–25). Here, we present a structural ensemble of ubiquitin based on an extensive

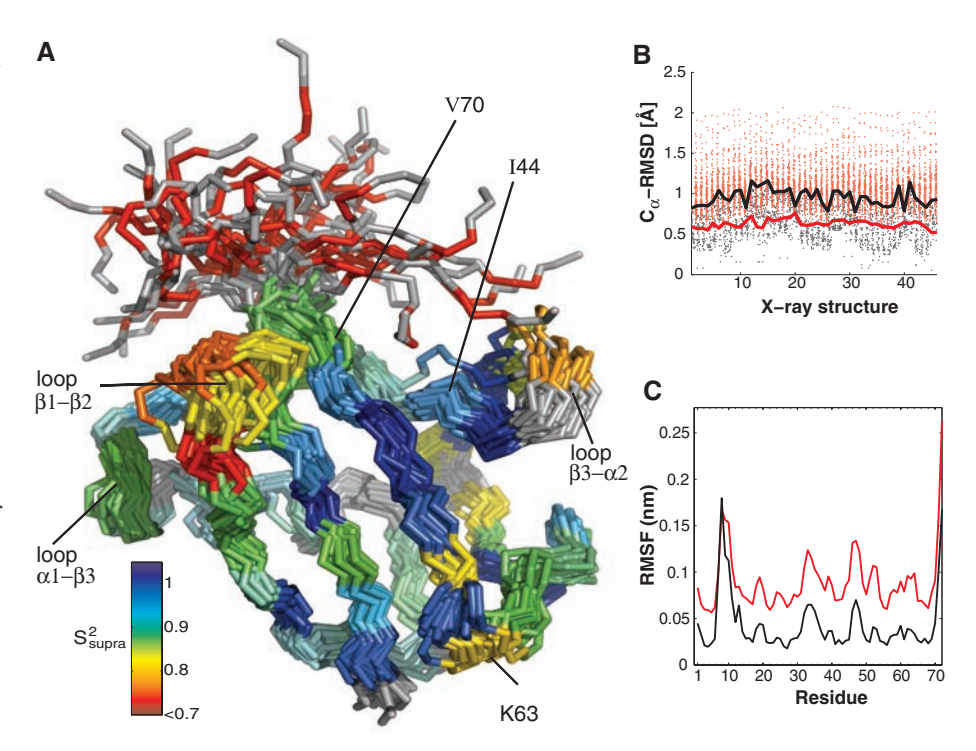


Fig. 1. Structure ensemble of ubiquitin. (**A**) Backbone trace of 40 randomly chosen structures from the EROS ensemble. Residues are colored by the amount of additional (supra- τ_c) mobility as compared with the Lipari-Szabo order parameters (Fig. 3C) $S_{\text{supra}}^2 = S_{\text{EROS}}^2/S_{\text{LS}}^2$. (**B**) For each x-ray structure (for numbering on the x axis, see table S3), the backbone RMSDs of residues 1 to 70 are shown for superpositions with each EROS structure (red dots) and each x-ray structure (black dots). The minimal RMSD for EROS structures (red line) and the maximal RMSD for x-ray structures (black line) are highlighted to guide the eye. (**C**) $C\alpha$ root mean square fluctuations (RMSF) of EROS structures (red line) and of 46 known ubiquitin x-ray structures (black line).

¹Department of Theoretical and Computational Biophysics, Max Planck Institute for Biophysical Chemistry, Am Fassberg 11, 37077 Göttingen, Germany. ²Department of NMR Based Structural Biology, Max Planck Institute for Biophysical Chemistry, Am Fassberg 11, 37077 Göttingen, Germany. ³Vanderbilt University Center for Structural Biology, Nashville, TN 37212, USA.

^{*}These authors contributed equally to this work. †To whom correspondence should be addressed. E-mail: cigr@nmr.mpibpc.mpq.de (C.G.); bgroot@qwdq.de (B.L.dG.)

RDC data set (Fig. 1). Ubiquitin is a key to many cellular signaling networks (26, 27) (as in protein degradation, for example) and is recognized by a broad variety of proteins with high specificity (28). Accordingly, ubiquitin crystal structures of 46 different complexes show a particularly pronounced structural heterogeneity (Fig. 2), which cannot be explained from the available sub- τ_c ensembles refined against NMR relaxation data (10, 11) (Fig. 2, C and E).

RDCs are observed in an anisotropic solution, induced (for example) by a highly diluted liquid crystalline medium (29) or a polyacryl amide gel. In such an anisotropic solution, the protein does not adopt all orientations with the same probability. Therefore, the rotational tumbling no longer averages the dipolar coupling to zero but to a measurable RDC. The anisotropic orientation distribution is represented by an alignment tensor, which is fixed to the molecular frame. For directly bonded nuclei, the RDC D depends only on the direction (θ,ϕ) of the internuclear vector in the alignment frame

$$D(\theta, \varphi) = D_a \Big[(3\cos^2 \theta - 1) + \frac{3}{2} R(\sin^2 \theta \cos 2\varphi) \Big]$$
 (1)

where $D_{\rm a}$ is the axial component of the alignment tensor and R describes its rhombicity (17, 29). Internal dynamics lead to orientational fluctuations of the internuclear vector (θ, ϕ) in the alignment frame (and therefore also in the molecular frame) and affect the size of the RDC according to Eq. 1. This variation of the RDC is usually in the range of less than 10 Hz, and therefore the RDC D is averaged to the measured $\langle D \rangle$ for motions faster than the upper limit of relaxation dispersion (10 ms), thus sampling the previously inaccessible supra- $\tau_{\rm c}$ time window.

Because the alignment tensor includes five parameters, the extraction of these fluctuations requires the measurement of RDCs in at least five independent alignment media. To assess the supra-τ_c time scale for ubiquitin, we measured RDCs for the backbone amide NH couplings in 18 different alignment conditions, as well as backbone H^NC' (amide proton to carbonyl carbon in the same peptide bond) and NC' (amide nitrogen to carbonyl carbon in the same peptide bond) RDCs from 4 different alignment media. Together with data from the literature (30-32), 36 NH RDC data sets and 6 HNC' and NC' RDC data sets were available. To probe side-chain dynamics as well, we included side-chain methyl group RDCs measured for 11 alignment media in the analysis (33).

Supra- τ_c ubiquitin ensemble reveals conformational selection. To extract a structural ensemble from these data, we carried out cross-validated ensemble refinement from unfolded structures in explicit solvent subjected simultaneously to restraints from NMR nuclear Overhauser enhancement (NOE) and RDC data (henceforth referred to as EROS for ensemble

refinement with orientational restraints). The unperturbed protein exhibits considerable flexibility, with a substantial fraction (color coded, Fig. 1A) attributed to supra- τ_c . Slower motions, at the microsecond-to-millisecond time scale, have previously been observed for only a very limited number of residues (34), thus confining the additional motion to the time range between the correlation time and about 50 μ s. As a crossvalidation, the ensemble was also calculated without NOEs. The resulting ensemble was found to be virtually unchanged [(33), EROS4], indicating that the ensemble is predominantly defined by the RDC data.

Unexpectedly, this supra- τ_c ensemble comprises the complete range of crystallographi-

cally observed structural changes during interface engagement (Figs. 1B and 2A), in contrast to the known fast dynamics (Fig. 2, C and E) (10, 11). Indeed, each of the x-ray structures is similar to members of the solution ensemble within less than 0.8 Å backbone root mean square deviation (RMSD) (Fig. 1B), although no crystallographic data have been used during refinement. Conformational selection, rather than induced fit, thus suffices to explain all known structural adaptations that the ubiquitin backbone undergoes upon complex formation with different binding partners. Remaining induced-fit motions are restricted to rotameric side-chain rearrangements and minor backbone changes.

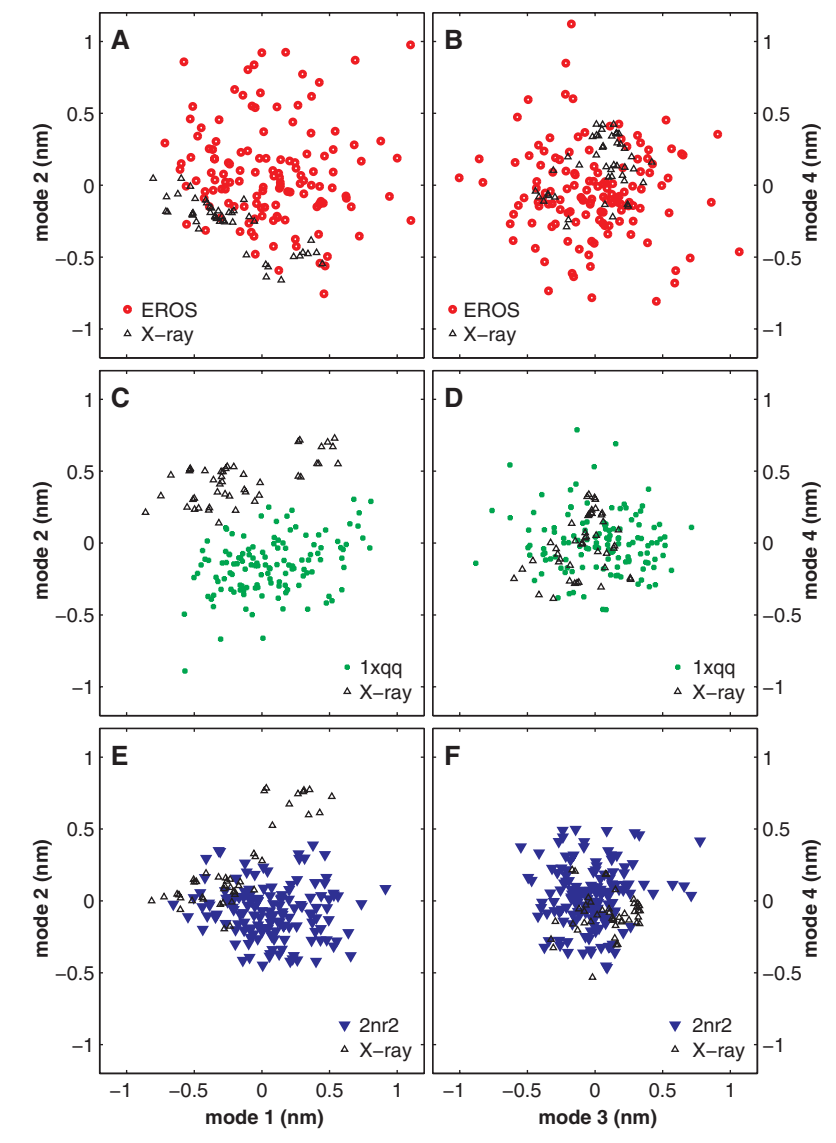


Fig. 2. Comparison of supra- τ_c and sub- τ_c solution ensembles (colors) with the collection of 46 x-ray structures (black) of ubiquitin by PCA: EROS (**A** and **B**), 1xqq (**C** and **D**), and 2nr2 (**E** and **F**). The PCA was carried out over the merged two ensembles that are displayed (in each case, the x-ray ensemble and one NMR ensemble: EROS, 1xqq, and 2nr2). Panels (A), (C), and (E) show projections onto the principal modes 1 and 2, whereas panels (B), (D), and (F) show projections onto modes 3 and 4. Systematic deviations are observed along the principal modes for both sub- τ_c ensembles but not for the supra- τ_c EROS ensemble.

As an independent validation of our ensemble, we have also applied a self-consistent RDC-based model-free (SCRM) analysis (33) to the set of 36 NH RDC experiments. This method is an enhanced implementation of the previously published model-free method (21, 24, 25) that largely alleviates structural bias (33). The SCRM analysis quantifies dynamics as the degree of orientational restriction of the amide NH bond in the molecular frame in terms of a generalized order parameter $S^2(NH)$, which is zero for complete isotropic disorder and one for a fixed orientation of the respective NH bond. For comparison, generalized order parameters were also computed from the EROS ensemble. A correlation coefficient r = 0.74 between S_{SCRM}^2 and S_{EROS}^2 is found (Fig. 3A). This agreement between two independent approaches shows that the dynamics observed in the EROS ensemble are indeed strongly determined by the experimental RDC data. This conclusion is supported by rigorous cross-validation implemented in EROS by systematically leaving out all RDCs between backbone amide N and carbonyl C, as well as all scalar couplings, from refinement. The ensemble-averaged free RDC R-factor of 18.5% is considerably lower than for other solution ensembles (>24%; table S2). Combining all xray structures into an "ensemble" (35), we obtained a similarly low R-factor of 18.3%. As compared with the R-factor of $25 \pm 4\%$ for individual x-ray conformers, this result confirms that the conformational heterogeneity (as found in the EROS ensemble and in the x-ray data) considerably improves the description of the experimental solution NMR data. In addition, the correlation between order parameters derived from the x-ray "ensemble," particularly when relaxed in short (10-ps) molecular dynamics simulations at 300 K [Fig. 3B; (33)],

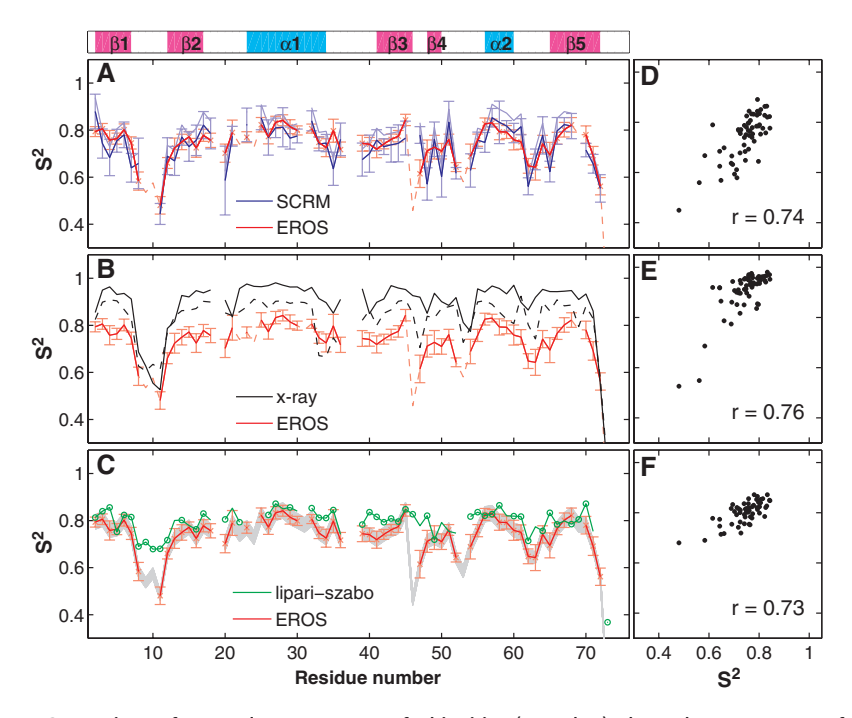


Fig. 3. Comparison of NH order parameters of ubiquitin. (A and D) The order parameters of the presented EROS ensemble (red) are compared with SCRM order parameters (blue) derived from the NH part of the RDC data used for EROS. The SCRM order parameters shown in dark blue reflect the most probable overall scaling with respect to the Lipari-Szabo-derived order parameters S_{LS}^2 . The most conservative scaling of SCRM order parameters to S_{LS}^2 is shown in light blue. (**B** and **E**) Order parameters intrinsic to the ensemble of 46 crystallographic structures (black). The dashed curve is obtained when the 46 structures are relaxed at 300 K by short molecular dynamics simulations of 10 ps. (C and F) Generalized order parameters obtained from NMR relaxation data (green) for the sub- τ_c dynamics of ubiquitin via Lipari-Szabo model-free analysis (36). Green circles mark the data points taken from the most recent and accurate measurement (36), whereas remaining data points are taken from previously published data (46). The latter (46) were rescaled such that they align with the newer results (36). The EROS order parameters were scaled by 0.93 to account for limited ensemble size and underestimation of the librational contribution (SOM text S4). Error bars (10) for the EROS ensemble (light-red) comprise intrinsic sampling and force-field errors as well as propagated experimental errors. The uncertainty in the libration correction was estimated as ±4% and is represented in gray. A solid line is shown for residues where sufficient RDC data were available to determine a robust value with SCRM analysis; for the other positions, EROS order parameters are shown as a dashed line. [(D) to (F)] Scatterplots for a direct comparison of the two sets of order parameters shown to the left of the respective plot.

and the RDC-derived order parameters $S_{\rm EROS}^2$ and $S_{\rm SCRM}^2$ suggests that the interconversion between the different ubiquitin conformations in the x-ray ensemble strongly contributes to the solution dynamics.

To assess how much of the solution dynamics is slower than τ_c , we compare S_{EROS}^2 and S_{SCRM}^2 with order parameters derived from NMR relaxation measurements. The picosecond-tonanosecond time scale dynamics of the ubiquitin backbone were probed previously by NMR relaxation techniques, yielding a set of S_{LS}^2 order parameters as derived from a Lipari-Szabo analysis (7, 36). Figure 3C compares order parameters $S_{\rm EROS}^2$ from the ensemble presented in Fig. 1A with S_{LS}^2 order parameters. For most residues, additional mobility is seen, thus quantifying the supra-τ_c motion in the EROS ensemble, shown as color code in Fig. 1A. For EROS, absolute order parameters were derived from the RDC-refined ensemble and corrected for limited ensemble size and libration effects. For SCRM analysis, the absolute scale was determined relative to S_{LS}^2 order parameters, with S_{LS}^2 as an upper bound for S_{SCRM}^2 , within the error bars [see supporting online material (SOM) text S1, section 1.2, and SOM text S4 for details]. Although the RDCs do not provide the absolute amplitude of the dynamics, the overall scale of the independently determined $S_{\rm EROS}^2$ and $S_{\rm SCRM}^2$ is nearly identical.

Solution fluctuations allow for interface contact formation. As noted above, the supra- τ_c motion accesses all the conformations that are observed in complex structures. To rationalize this unexpected result, we overlaid all interface-contacts (gray spheres) of the different binding partners found in the x-ray structures with a single structure of ubiquitin whose coloring represents the solution dynamics as given by $S_{\text{EROS}}^2(\text{NH})$ (Fig. 4A). Notably, helix α1, for which no contacts are observed, shows only little motion in solution (blue), whereas high flexibility (orange-red) is observed in regions that form many different protein-protein interfaces. A quantitative analysis of the number of interface contacts per residue (Fig. 4C) shows an unexpectedly high similarity to the conceptually unrelated order parameters $S_{\rm EROS}^2({\rm NH})$, which corroborates this initial observation.

Two prominent exceptions from the observed high flexibility in the binding regions are residues Ile^{44} and His^{68} [I44 and H68 (37)] (two of the three "x" symbols in Fig. 4C). Both are known from mutation studies to be central hotspot (38) residues of a binding motif (Fig. 4B) that is involved in recognition of many different binding partners (26, 39). Recently, the first crystal structure with a new recognition motif centered at hotspot D58 (one of the three "x" symbols in Fig. 4C) has been found (40). Our results show that, in solution, this residue is as rigid as I44/F45 and H68.

At first sight, the observed fluctuations appear incompatible with the proposed conformational

selection scenario. In particular, it seems combinatorially highly unlikely to find all involved residues simultaneously in the proper configuration required for binding, thus imposing a high entropic barrier. Only concerted fluctuations, implying reduced entropic cost, would explain the observed high physiological on-rates and affinities (39).

Collective molecular recognition dynamics. To check whether such concerted fluctuations are actually observed in the ubiquitin ensemble, we have carried out a principal component analysis (PCA). The conformational changes observed in x-ray structures are well described within the first five principal components. Although the number of degrees of freedom is reduced from 1839 to only 5, all x-ray structures can be described up to a backbone RMSD of 0.45 ± 0.04 Å. From linear combinations of these five principal components, we found a single collective mode that corresponds to a pincer-

like motion of predominantly those residues that are frequently involved in interfaces and accounts for 25% (RMSD) of all backbone fluctuations in the solution ensemble (Fig. 5B).

Whether this mode indeed describes the molecular recognition dynamics can be tested stringently by predicting the bound ubiquitin conformations with the use of information only from the binding partner. To this end, we systematically varied the ubiquitin structure along this mode for each of altogether 41 interfaces, until the highest number of contacting interface atoms (i.e., atoms within 3 to 8 Å of the binding partner) was reached. A correlation of 0.94 between the projection of the thus predicted and the actual x-ray structure was found for the pincer-like mode (Fig. 5A). Analogously, correlations of 0.90 and 0.84 were obtained for the linearly combined first three principal components and for the third principal component, respectively. These

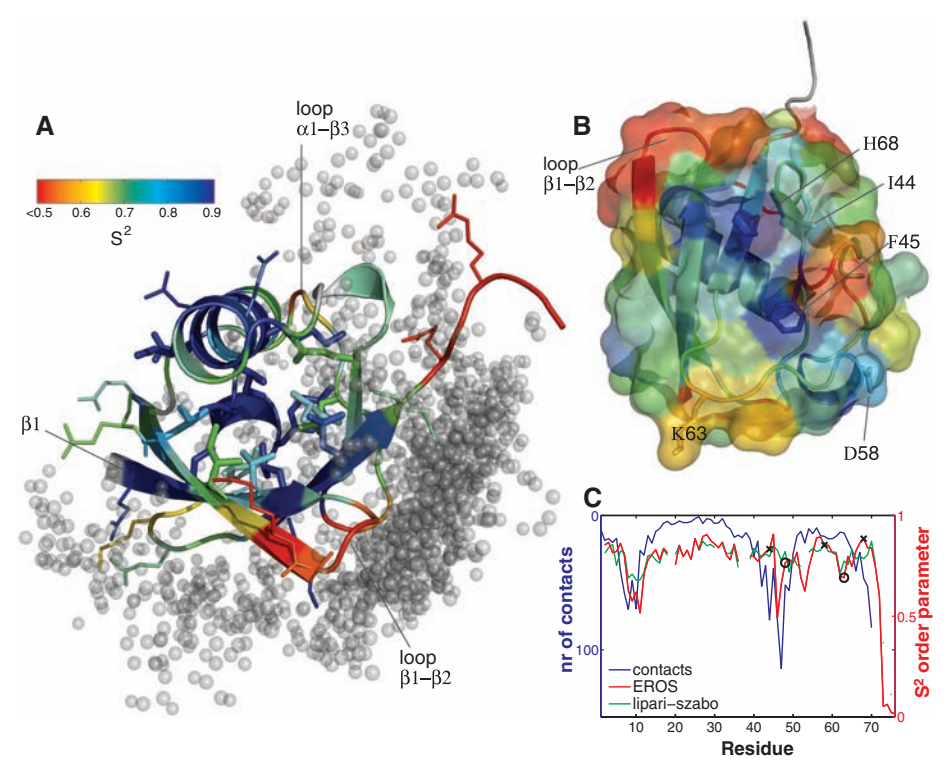


Fig. 4. Solution dynamics correlate with molecular recognition sites. (**A** and **B**) The apo structure of ubiquitin (1UBI) is colored by backbone flexibility in solution as given by S_{EROS}^2 . (A) Positions of contacting atoms of complexing proteins (<5 Å distance) are shown as gray spheres. (B) View toward the surface at the most prominent recognition site around residues I44/H68. H68 (sticks) lies within a rigid crevice that connects via F45 to the other known recognition site centered at D58. The walls of this crevice are formed by regions with high flexibility. Around H68, rigidity is provided by packing of core residues L67 and L69 (not shown) against the central helix; at D58, packing of L55 and a long-range hydrogen bond from Y59 to E51 provide stability. (**C**) Number (nr) of ubiquitin-binding protein contacts per residue (blue line) and the flexibility in solution for the sub-τ_c time regime (green line) and the supra-τ_c time range, as extracted from the EROS ensemble (red line). A marked correlation between contacts and solution fluctuations is observed, particularly for the EROS ensemble. Exceptions from the observed correlation are found for known molecular recognition hotspots (marked with "x" symbols: I44/H68, D58), which may act as rigid anchors, allowing flexibility for neighboring residues. Lysines responsible for polyubiquitination are marked with circles (K48, K63).

consistently high correlations for collective modes indicate that the interface adaptation dynamics of ubiquitin are indeed well described within a few collective degrees of freedom that dominate the solution ensemble. Moreover, this analysis indicates that the ability to optimize contacts with binding partners via backbone interface adaptation is important for ubiquitin to reach sufficient affinity with many different binding partners. As illustrated in Fig. 5B, for the ubiquitin interfaces with hepatocyte growth factor-regulated tyrosine kinase substrate (HRS) and the zinc finger ubiquitin-binding domain of isopeptidase T [Protein Data Bank (PDB) accession codes 2D3G and 2G45], the collective solution mode allows molecular recognition by enabling ubiquitin to adapt to different protein interfaces.

The slow supra- τ_c time scale of ubiquitin's interface adaptation dynamics is corroborated by the observation that collective solution modes obtained from the first five principal components of nanosecond ensembles 1xqq and 2nr2 (10, 11) were less adept in describing the interface adaptation. For these modes, the correlation between predicted and crystallized position dropped from 0.94 to 0.68 and to 0.55, respectively. The supra- τ_c time scale has previously been speculated to be important in the context of signal propagation of the immunoglobulinbinding domain of protein G (20) as well as for aggregation dynamics (41).

Summary. Taken together, we have determined a solution ensemble of a globular protein from experimental data that comprises all solution dynamics up to the microsecond time scale at atomic resolution. A large part of this solution dynamics is concentrated in a collective pincer-like motional mode that strongly contributes to the interface adaptation dynamics during molecular recognition events. All available crystallographic structures of ubiquitin complexed to different binding proteins were shown to be accessible in solution. Conformational selection, rather than induced fit, is thus the main contributor to the observed interface adaptations. The observed conformational selection dynamics lower entropic barriers, thereby explaining physiologically observed high affinity and fast on-rates which otherwise would need to be explained by induced-fit motions.

These findings suggest how ubiquitin recognizes many different partner proteins with a high degree of specificity and sufficient affinity. In order to reach sufficient affinity, a certain degree of structural plasticity is required that is thermally accessible in solution. In order to maintain high specificity despite the inherent flexibility, the binding interfaces are centered around the rigid hotspot (38) residues H68/I44 and D58. The rigidity of these mutational hotspots (26, 39, 40) might prevent promiscuous binding, because only precisely aligned

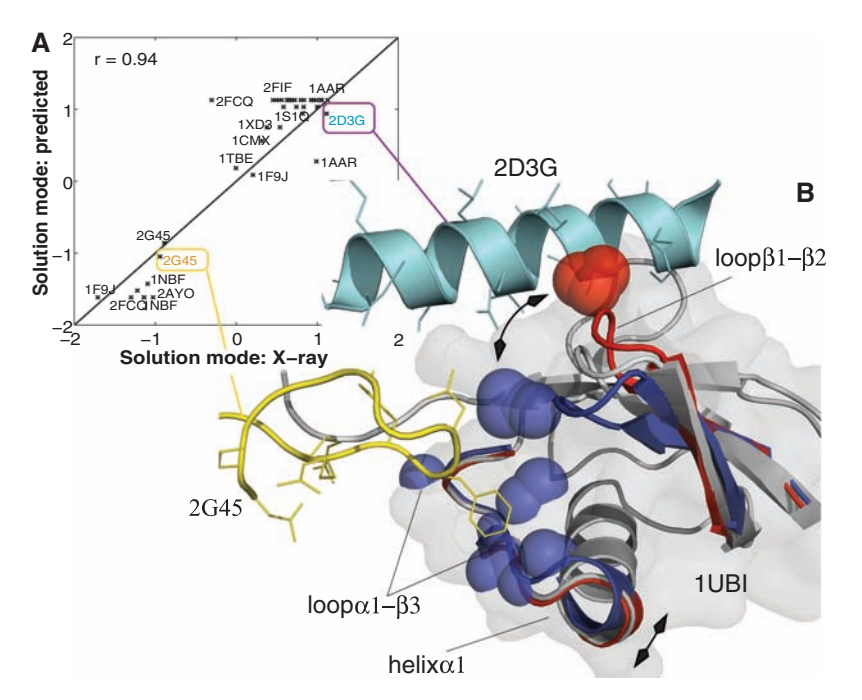


Fig. 5. Equilibrium supra- τ_c dynamics are dominated by conformational selection dynamics. A large amplitude collective solution mode entails a pincer-like motion of loop $\beta 1$ - $\beta 2$ and loop $\alpha 1$ - $\beta 3$ including the C-terminal tip of helix $\alpha 1$. For each of altogether 41 binding partners, this collective solution mode was systematically varied to find a predicted position that maximized contacts. (**A**) The position on the mode of the thus predicted selected structures is plotted on the y axis, whereas the projected position onto this mode for the actual crystal structures is plotted on the x axis. (**B**) In order to illustrate the conformational selection along the collective solution mode, two of the selected snapshots (dark blue and red) are shown together with relevant parts of their respective binding partners: the zinc finger ubiquitin-binding domain of isopeptidase T (2G45, yellow) and HRS (2D3G, cyan). Contacts affected by the motion along the collective mode are shown as spheres. The crystal structure of 1UBI is shown at relevant regions as a gray cartoon. The full protein is shown as a semitransparent surface.

partner interfaces benefit from the high hotspot energy contribution. Structurally, the observed rigidity is maintained for H68 by packing with its neighbors L67 and L69 tightly into the protein core, whose rigidity is reinforced by helix 1. Similarly, I44 is anchored via F45 and decoupled from the adjacent flexible loop via an alanine-glycine linker (A46/G47). At D58, packing of L55 and a long-range hydrogen bond from Y59 to E51 provide stability. Because the solution dynamics are dominated by the collective pincer-like interface adaptation, it seems that only functionally essential flexibility is present. Apparently, ubiquitin has evolved to be as rigid as possible while remaining as flexible as necessary to engage in different interfaces.

Our finding that conformational selection is responsible for protein-protein binding of ubiquitin is in line with recent findings of conformational selection occurring for antibodies and enzymes (42–44). For the latter, relaxation dispersion experiments that are sensitive to microsecond-to-millisecond time scales (i.e., 1000 times slower than the processes we described here) show conformational selection for all steps in enzymatic reactions of dihydrofolate reductase (9). It should be noted that our

findings differ from the stepwise model proposed for the binding of unfolded proteins to folded ones (45) and thus open up a whole range of possible molecular recognition mechanisms.

References and Notes

- C. Kolano, J. Helbing, M. Kozinski, W. Sander, P. Hamm, Nature 444, 469 (2006).
- H. Frauenfelder, P. G. Wolynes, Science 229, 337 (1985).
- 3. A. Mittermaier, L. E. Kay, Science 312, 224 (2006).
- L. E. Kay, D. A. Torchia, A. Bax, Biochemistry 28, 8972 (1989).
- 5. M. Akke, A. Palmer, J. Am. Chem. Soc. 118, 911 (1996).
- L. Wang et al., Proc. Natl. Acad. Sci. U.S.A. 98, 7684 (2001).
- G. Lipari, A. Szabo, J. Am. Chem. Soc. 104, 4546 (1982).
- 8. K. A. Henzler-Wildman et al., Nature 450, 913 (2007).
- 9. D. D. Boehr, D. McElheny, H. J. Dyson, P. E. Wright, Science **313**, 1638 (2006).
- K. Lindorff-Larsen, R. B. Best, M. A. DePristo, C. M. Dobson, M. Vendruscolo, *Nature* 433, 128 (2005).
- B. Richter, J. Gsponer, P. Varnai, X. Salvatella, M. Vendruscolo, J. Biomol. NMR 37, 117 (2007).
- M. Akke, R. Bruschweiler, A. G. Palmer, J. Am. Chem. Soc. 115, 9832 (1993).
- 13. D. Yang, Y.-K. Mok, J. D. Forman-Kay, N. A. Farrow, L. E. Kay, *J. Mol. Biol.* **272**, 790 (1997).
- K. K. Frederick, M. S. Marlow, K. G. Valentine, A. J. Wand, Nature 448, 325 (2007).
- C. S. Goh, D. Milburn, M. Gerstein, Curr. Opin. Struct. Biol. 14, 104 (2004).

- 16. R. Grunberg, J. Leckner, M. Nilges, *Structure* **12**, 2125 (2004).
- J. R. Tolman, J. M. Flanagan, M. A. Kennedy,
 J. H. Prestegard, *Proc. Natl. Acad. Sci. U.S.A.* 92, 9279 (1995).
- 18. J. R. Tolman, J. Am. Chem. Soc. 124, 12020 (2002).
- N. A. Lakomek et al., Angew. Chem. Int. Ed. 44, 7776 (2005).
- G. Bouvignies et al., Proc. Natl. Acad. Sci. U.S.A. 102, 13885 (2005).
- N. A. Lakomek, T. Carlomagno, S. Becker, C. Griesinger,
 Meiler, J. Biomol. NMR 34, 101 (2006).
- G. Bouvignies, P. Markwick, R. Bruscheweiler, M. Blackledge, J. Am. Chem. Soc. 128, 15100 (2006).
 R. B. L. Markwick, G. Pourignios, M. Plackledge, J. Am.
- P. R. L. Markwick, G. Bouvignies, M. Blackledge, J. Am. Chem. Soc. 129, 4724 (2007).
- J. Meiler, J. J. Prompers, W. Peti, C. Griesinger,
 R. Bruschweiler, J. Am. Chem. Soc. 123, 6098 (2001).
- 25. W. Peti, J. Meiler, R. Bruschweiler, C. Griesinger, *J. Am. Chem. Soc.* **124**, 5822 (2002).
- L. Hicke, H. L. Schubert, C. P. Hill, Nat. Rev. Mol. Cell Biol. 6, 610 (2005).
- 27. J. W. Harper, B. A. Schulman, Cell 124, 1133 (2006).
- 28. P. S. Brzovic, R. E. Klevit, Cell Cycle 5, 2867 (2006).
- 29. N. Tjandra, A. Bax, Science 278, 1111 (1997).
- K. B. Briggman, J. R. Tolman, J. Am. Chem. Soc. 125, 10164 (2003).
- 31. K. Ruan, J. R. Tolman, *J. Am. Chem. Soc.* **127**, 15032 (2005).
- 32. M. Ottiger, A. Bax, J. Am. Chem. Soc. **120**, 12334 (1998).
- 33. See supporting material on Science Online.
- F. Massi, M. J. Grey, A. G. Palmer, *Protein Sci.* 14, 735 (2005).
- R. B. Best, K. Lindorff-Larsen, M. A. DePristo, M. Vendruscolo, Proc. Natl. Acad. Sci. U.S.A. 103, 10901 (2006).
- S. L. Chang, N. Tjandra, J. Magn. Reson. 174, 43 (2005).
- Single-letter abbreviations for the amino acid residues are as follows: A, Ala; C, Cys; D, Asp; E, Glu; F, Phe; G, Gly; H, His; I, Ile; K, Lys; L, Leu; M, Met; N, Asn; P, Pro; Q, Gln; R, Arg; S, Ser; T, Thr; V, Val; W, Trp; and Y, Tyr.
- 38. T. Clackson, J. A. Wells, Science 267, 383 (1995).
- 39. C. Kiel, L. Serrano, *J. Mol. Biol.* **355**, 821 (2006).
- 40. L. Penengo et al., Cell 124, 1183 (2006).
- 41. C. W. Bertoncini *et al.*, *Proc. Natl. Acad. Sci. U.S.A.* **102**, 1430 (2005).
- 42. E. Z. Eisenmesser et al., Nature 438, 117 (2005).
- 43. C. Tang, C. D. Schwieters, G. M. Clore, *Nature* **449**, 1078 (2007).
- L. C. James, P. Roversi, D. S. Tawfik, Science 299, 1362 (2003).
- K. Sugase, H. J. Dyson, P. E. Wright, Nature 447, 1021 (2007).
- 46. N. Tjandra, S. E. Feller, R. W. Pastor, A. Bax, *J. Am. Chem. Soc.* **117**, 12562 (1995).
- 47. We thank A. Munk for suggesting a scaling method for the SCRM order parameters; F. Mulder, A. Bonvin, and N. Tjandra for discussion of the overall scaling of Lipari-Szabo order parameters; K. Giller for the preparation of numerous labeled ubiquitin samples; and A. Mark, K. Riebeseel, E. d'Auvergne, L. Joachimiak, and M. Tyka for carefully reading the manuscript and fruitful discussions. This work was supported by the Max Planck Society (to H.G., C.G., and B.L.dG.), the Fonds der Chemischen Industrie (to C.G.), the German Israel Foundation (to C.G.), the Human Frontier Science Program (to O.F.L.), and the Volkswagen Foundation (to O.F.L.). Coordinates and RDCs have been deposited in the PDB (www.rcsb.org) with the accession number 2k39.

Supporting Online Material

www.sciencemag.org/cgi/content/full/320/5882/1471/DC1 SOM Text S1 to S7

Figs. S1 to S9

Tables S1 to S8

References

28 February 2008; accepted 2 May 2008 10.1126/science.1157092



Supporting Online Material for

Recognition Dynamics Up to Microseconds Revealed from an RDC-Derived Ubiquitin Ensemble in Solution

Oliver F. Lange, Nils-Alexander Lakomek, Christophe Farès, Gunnar F. Schröder, Korvin F. A. Walter, Stefan Becker, Jens Meiler, Helmut Grubmüller, Christian Griesinger,* Bert L. de Groot*

*To whom correspondence should be addressed. E-mail: cigr@nmr.mpibpc.mpg.de (C.G.); bgroot@gwdg.de (B.L.dG.)

Published 13 June 2008, Science 320, 1471 (2008)

DOI: 10.1126/science.1157092

This PDF file includes:

SOM Text S1 to S7 Figs. S1 to S9 Tables S1 to S8 References

1. METHODS

1.1. EROS. Three different types of starting structures for EROS refinement were used in this work, resulting in ensembles termed EROS, EROS2, EROS3 and EROS4. For the ensemble denoted EROS and EROS4, ubiquitin structures were subjected to ensemble treatment from scratch. To this aim, starting from random coordinates, the CONCOORD program[1] was used to generate pairs of ubiquitin structures that together fulfil measured NOE data[2]. The resulting structures are based on a minimal geometrical model of bond lengths and angles and van der Waals radii, together with sum-averaged NOE-based distance bounds. Sum averaging was applied as $\overline{r_{kl}^{-6}}=\frac{1}{2}\sum_{j=1}^2 r_{kl,j}^{-6}$, corresponding to time scales beyond the supra- τ_c time scale. 500 of such structure pairs were generated. Of these 1000 structures, the 400 best matching the RDC data (in sub-ensembles of 2 structures) were used for further refinement (see below). After refinement, the same selection was repeated once more to select the best 400 sub-ensembles of 2 structures (allowing duplication). Each structure that was selected at least once by the second filter step was added to the final ensemble. Cross-validation showed that R_{free} did not decrease with further refinement/selection cycles. In all selection rounds, only the non-NC couplings were used as working set, allowing cross-validation using NC couplings. From the final ensemble of 132 structures, 16 were removed due to chirality violations, leaving 116 conformers.

To assess the influence of the choice of starting structures, refinement was also carried out with all refinements started from one single configuration, the first entry in the high-resolution NMR ensemble 1d3z. This resulted in the EROS2 ensemble. Similarly, for EROS3, 400 initial structures were generated using CONCOORD that fulfil the NOE restraints in each single configuration.

To assess the impact of NOEs on the refinement, the EROS4 ensemble was started from the same structural pool as EROS with the difference that during refinement against RDC data no NOE restraints were applied.

Refinement was carried out using the GROMACS simulation package[3, 4]. Ensemble refinement was carried out by simultaneously applying NOE and RDC restraints on subensembles of eight structures, as cross-validation indicated eight as the optimal ensemble size. All refinement simulations were carried out using simulated annealing in explicit solvent and periodic boundary conditions. The initial temperature was set to 350K and

slowly cooled to 0K during 100 ps, after which the temperature was raised to 310K during 10 ps. This annealing protocol was chosen as cross-validation indicated that it yields favorable results. Particle Mesh Ewald (PME) was used to describe long-range electrostatic interactions[5, 6]. Unless indicated otherwise, the OPLS/AA-L all-atom force-field[7] and the SPC water model[8] were applied. For the EROS and EROS3 ensembles, 3000 water molecules were used, for the EROS2 ensemble 4107. All simulations were run at constant volume. In addition to the OPLS/AA-L force field, EROS3 ensembles were also refined using the charmm-27[9], the amber03[10, 11], and the gromos96-53a6 force fields[12]. For the simulations carried out in the charmm-27 and amber03 force fields, TIP3P[13] was used as water model instead of SPC. Lincs[14] was used to constrain bond-lengths, allowing a time step of 2 fs. For bonds involving RDCs, bond lengths were chosen as d(H-N)=1.04 Å; d(CA-HA)=1.12 Å; d(N-C)=1.33 Å; d(CA-C)=1.53 Å[15]. Other bond lengths were taken from the respective force fields. Force constants of 1000 kJ/ (mol nm²) and 0.25 kJ/ (mol Hz²) were chosen for NOEs and RDCs, respectively. For each RDC experiment one alignment tensor was determined from eight structures for every time step during refinement, after superimposing the backbone atoms of residues 1–70 onto each other.

Sum averaging $\overline{r_{kl}^{-6}} = \frac{1}{8} \sum_{j=1}^{8} r_{kl,j}^{-6}$ during EROS refinement ensured that the NOE restraints are solely imposed on structure ensembles rather than individual structures, allowing individual structures to violate the NOE distance bounds. It is well established that r^{-6} averaging allows for substantial flexibility for individual atom pairs involved in NOEs, even in ensembles of only two structures[16, 17]. Such large flexibility, up to local partial unfolding, was indeed observed in the NOE-based ensemble consisting of 2-membered NOE-sub-ensembles that was used as starting point for EROS refinement. It was found that the flexibility of the RDC-refined ensemble (with a mean ensemble backbone RMSD of 1.22 Å, and a maximum of 2.53 Å) is considerably lower than that of the NOE-based ensemble that served as starting ensemble for RDC refinement (mean RMSD: 1.83 Å; max.: 4.85 Å). Hence, the structures and flexibility in the refined ensemble are to a large extent determined by the RDCs. This notion is further corroborated by the fact that the sum of NOE violations (summed over all 2727 NOE's in the 1d3z dataset) is as low as 0.66 nm in the EROS4 ensemble, in which no NOE restraints were applied (compared to 0.11 nm in the EROS ensemble, in which NOE restraints were included).

Order parameters S^2_{EROS} of the EROS ensembles were computed after superimposing the backbone atoms of residues 1-70 onto each other. Expressing the orientation of the NH vectors of the superimposed structures in spherical coordinates (θ, φ) the order parameters were obtained as

$$S^{2} = \frac{4\pi}{5} \sum_{M=-2}^{2} \langle Y_{2M} \left(\theta, \varphi \right) \rangle \langle Y_{2M}^{*} \left(\theta, \varphi \right) \rangle,$$

where the Y_{2M} denote the normalized second-order spherical harmonic functions $Y_{20}\left(\theta,\varphi\right)=\sqrt{5/\left(16\pi\right)}\left(3\cos^{2}\theta-1\right), Y_{2\pm1}\left(\theta,\varphi\right)=\mp\sqrt{15/\left(8\pi\right)}e^{\pm i\varphi}\cos\theta\sin\theta$, and $Y_{2\pm2}\left(\theta,\varphi\right)=\sqrt{15/\left(32\pi\right)}e^{\pm2i\varphi}\sin^{2}\theta$.

As a hybrid protocol between the model-free SCRM method (see below) and EROS refinement, we developed a minimal geometrical model. Structurally, it contains solely bond length and weak bond angle terms, together with a minimal set of van der Waals radii (chosen as 0.13, 0.14, 0.16, 0.16 and 0.05 nm for O, N, C, S, and H, respectively). Compared to the molecular mechanics force fields used in EROS, therefore, torsion angles, dispersion interactions, electrostatic interactions, and solvent interactions are neglected. In addition, this 'geometry filter' shares the method to determine the alignment tensor with the SCRM approach: the NH vectors of the protonated 1UBQ X-ray structure were rotated iteratively to optimally match the NH RDCs. The according alignment tensor was subsequently used in ensemble refinement.

1.2. **Self-Consistent RDC-based Model-free (SCRM).** Order parameters derived from the EROS ensemble method were compared to RDC-based order parameters independently derived by the Self-Consistent RDC-based Model-free (SCRM) method. The SCRM approach allows determination of internal protein dynamics from RDCs largely without structural noise and determines the dynamic average orientation of the inter-nuclear vectors in the protein structure. Removing structural noise from the model-free analysis therefore further increases the accuracy of this analysis and allows more accurate statements about the supra- τ_c motion, i.e. motion beyond the correlation time to be made. The approach relies on the previously introduced model-free approach[18, 19]. Based on a set of dipolar couplings and a static input structure, alignment tensors and dynamically averaged spherical harmonics describing the average orientation of each NH vector as well as its dynamics were derived. The key of the self-consistent analysis is to take output average orientations

as input of the next tensor calculation and repeat until convergence is reached. The iteration is stopped when the order parameters between subsequent cycles agree within 0.01.

The SCRM method yields a relative estimate of RDC-based order parameters, e.g., of NH bond vectors. As the absolute scale of the SCRM order parameters is unknown, they are usually scaled with respect to Lipari-Szabo (LS) relaxation order parameters[19, 20]. This approach rests on the assumption that at least a few residues will show little additional dynamics beyond the overall tumbling time scale, and hence yields a conservative estimate of the overall level of supra- τ_c motion. The optimal relative scaling is non-trivial, and we have therefore developed two independent methods to obtain a scaling estimate.

Scaling method S1 is based on hypothesis tests. In a first step, S1 was applied to test the hypothesis that the LS order parameters and SCRM order parameters (at any scaling) stem from the same distribution (zero supra- τ_c motion hypothesis). This was achieved by generating multiple sets of synthetic order parameters, Gaussian-distributed around the measured SCRM order parameters with a standard deviation given by the respective uncertainties. The zero supra- τ_c motion hypothesis was rejected with a confidence of more than 99.999%, indicating significant supra- τ_c motion. To obtain a scaling estimate, in a second step, the method successively removes residues that display the most significant supra- τ_c motion until the zero supra- τ_c motion hypothesis cannot anymore be rejected for the remaining residues at a confidence level above 95%. The corresponding scale that optimally scales the remaining SCRM order parameters to the respective LS order parameters is the suggested scaling factor. This method is similar in spirit to the step-fitting algorithm recently proposed for microtubule growth[21].

Uncertainties in order parameters were estimated via error propagation both from the experimental error on the RDCs (0.3 Hz), and from the post-SCRM[22] RDC rmsd (0.52 Hz), yielding scaling factors $S_{\rm Overall}^2$ of 0.88 and 0.91, respectively, which were applied to the SCRM curves shown in Fig. 3.

An alternative scaling method S2 was developed to allow the comparison with the scaling derived by the S1 method. Scaling method S2 is based on the notion that the true RDC-based order parameters must be strictly smaller than corresponding LS order parameters, due to the longer time scales probed by RDCs. As the SCRM order parameters are determined with a certain experimental uncertainty, the scaling of the SCRM order parameters

	X-ray	heated X-ray	Lipari Szabo	SCRM	EROS
X-ray	X				
heated X-ray	0.71	X			
Lipari Szabo	0.46	0.40	X		
SCRM	0.65	0.50	0.41	X	
EROS	0.76	0.73	0.73	0.74	х
geometry filter	0.7 (0.74)	0.52 (0.56)	0.56 (0.61)	0.82 (0.86)	0.84 (0.87)

TABLE S1. correlation of S^2 (NH) order parameter. The correlation coefficients for the row *geometry filter* reflect the mean over 50 geometry filter ensembles; the mean of the best correlating 10% is given in brackets.

to strictly obey this condition for all residues (with the highest one equal to LS) would underestimate the scaling factor. In order to alleviate this bias, the amount of underestimation thus produced is estimated from a set of synthetic order parameters, Gaussian-distributed around the measured SCRM order parameters, with a standard deviation corresponding to the respective uncertainty. These synthetic data are scaled such that they are strictly below the LS order parameters, with the highest one equal to the corresponding LS value. The distribution of these synthetic scaling factors then allows the estimation of confidence intervals of the originally measured set of SCRM order parameters. Scaling factors derived from 95% confidence intervals (i.e., 95% of the scaling factors are smaller than the suggested scale) were used to derive the best estimate for the scaling factors. The 95% confidence interval scaling factors corresponding to 0.30 Hz and 0.52 Hz RDC uncertainties are 0.89 and 0.93, respectively, showing agreement to the estimates from method S1[22].

2. COMPARISON OF SCRM AND EROS ORDER PARAMETERS

As presented in the main text, the order parameters obtained from the RDC data with our model-free approach $S^2_{\rm SCRM}$ agree with $S^2_{\rm EROS}$ within error. This agreement is remarkable considering the many differences between the two approaches. It shows that the dynamics observed in the EROS ensemble is strongly determined by the experimental residual dipolar coupling data (cf. Table S1).

The agreement between $S^2_{\rm SCRM}$ and $S^2_{\rm EROS}$ is observed despite potential force-field bias or sampling problems in the EROS protocol, or due to inclusion of solutions in the model-free approach that are geometrically unfeasible. To evaluate the effect of some of the potential assumptions, we hybridized the two approaches by coupling the alignment procedure

of the model-free approach with a minimal geometrical structural model of ubiquitin that only restricts bond lengths and avoids clashes of atoms (see sec. S1.1). Both, the EROS and model-free results agree well with order parameters obtained by this hybrid approach (r=0.84 and 0.82 respectively). Furthermore, the particular choice of molecular mechanics force-fields affects the obtained EROS order parameters only slightly, as shown by an average mutual correlation of r=0.88 between EROS solutions obtained with four different state of the art force-fields (see also Section S6.2). This indicates that the agreement between EROS and SCRM order parameters is robust independently of how the results are obtained.

3. Cross-validation

The EROS ensemble was cross-validated by systematically leaving out data from the refinement. All RDCs between backbone amide N and carbonyl C, as well as all scalar couplings were used for this purpose.

R-values,

$$R_{\mathrm{X}} = \left(\Sigma_{k}^{n_{x}} \left(\mathbf{X}_{\mathrm{k,calc}} - \mathbf{X}_{\mathrm{k,exp}} \right)^{2} / \left(2 \sum_{k}^{n_{x}} \mathbf{X}_{\mathrm{k,exp}}^{2} \right) \right)^{1/2},$$

for data class X (e.g., an experiment) with $n_{\rm x}$ data points and Pearson correlation coefficients $R_{\rm X}$ were computed individually for every data-class and subsequently averaged. For RDCs, a data-class comprises all couplings between the same type of nuclei determined in the same alignment medium. For scalar couplings the data classes are HNHA, HNCO, HNCB, COHA, COCO, and COCB for the backbone φ -dihedral and the two N- C_{γ} , C'- C_{γ} for the side chain χ_1 -dihedral, respectively[2]. R-values were averaged as

$$R = \left(\sum_{j=1}^{N} n_{j}\right)^{-1/2} \left(\sum_{i=1}^{N} n_{i} R_{i}^{2}\right)^{1/2},$$

where N denotes the number of data-classes. Correlation coefficients were arithmetically averaged. All R-values represented are $R_{\rm free}$, if not otherwise stated. RDC cross-validation was carried out via amide NC' RDCs obtained in 6 alignment media. The alignment tensor used to compute the NC'-RDCs has been fitted via all non-NC' RDCs.

The ensemble averaged "free" RDC R-factor is 18.5%. This is substantially lower than the values obtained for a single X-ray structure $(25\pm4\%)$, the NMR ensemble 1d3z (24%) or for the previously published ensembles aimed at describing nanosecond dynamics 1xqq

(27.9%) and 2nr2 (24.1%). The value obtained for the ensemble of X-ray structures is 18.3%. This finding shows that conformational heterogeneity as found in the EROS ensemble or in the ensemble of 46 X-ray structures considerably improves the description of the experimental data with respect to individual structures (the lowest value observed for any of the individual X-ray conformers was 20.4%). Moreover, the conformational heterogeneity found in the nanosecond ensembles (1xqq and 2nr2) does not improve the description of the RDC data over a single X-ray structure. Scalar couplings in the backbone and in the side-chain, as well as scalar couplings across hydrogen bonds are described well by the EROS ensemble. The $R_{\rm free}$ value of 18.5% for the EROS ensemble indicates that potential model bias and over-fitting issues are acceptable. Moreover, it indicates that alignment media have minimal influence on the structure and ensemble of ubiquitin.

Ensemble	$R_{\text{free}}\left(^{3h}J_{NC;}\right)$	$R_{\text{free}}\left(^{3}J_{\varphi}\right)$	$R_{\text{free}}\left(^{3}J_{\chi_{1}}\right)$	$R_{\mathrm{free}}\left(\mathrm{RDC}\right)$
EROS	0.19	0.20	0.10	0.185
EROS2	0.19	0.20	0.10	0.188
EROS4	0.19	0.21	0.10	0.190
X-ray46	$0.25^{3,5}$	0.15	0.10	$0.182^{3,5}$
1xqq	0.21	0.27	0.09	$0.279^{5,6}$
1d3z	0.25 2	0.17 1	0.14	0.242^{1}
2nr2	0.18	0.25	0.10	$0.241^{5,6}$
1ubi	0.35^{3}	0.18	0.19	0.24^{3}
EROS_avg ⁴	0.29	0.23	0.17	0.27

(b):

Ensemble	$r\left(^{3h}J_{NC;}\right)$	$r(^3J_{\varphi})$	$r(^3J_{\chi_1})$
EROS	0.81	0.94	0.97
EROS2	0.81	0.93	0.97
EROS4	0.81	0.93	0.97
X-ray46	0.85^{3}	0.94	0.98
1xqq	0.77	0.88	0.98
1d3z	0.69	0.93 1	0.95
2nr2	0.85	0.88	0.97
1ubi	0.72^{3}	0.92	0.88
EROS_avg ⁴	0.78	0.94	0.90

TABLE S2. Cross-validation of ubiquitin structures via scalar couplings. (a) RDC R-factors and (b) pearson correlation coefficients. ¹some of the data was used during the refinement[2]. ²one outlier was removed. ³Protons were placed with molecular modelling package whatIF[23]. ⁴Average structure computed from EROS ensemble. ⁵For bonds involving RDCs bond lengths were set to the same lengths chosen for EROS[15] using the Lincs algorithm[14]. ${}^6R_{\text{free}}$ of ensembles 1xqq and 2nr2 as originally deposited, i.e., without bond length correction, is 0.296 and 0.262, respectively. For 1d3z the value differs from the $16\%/\sqrt{2} = 11\%$ reported in Ref. [2]. The reason for this discrepancy is that here the evaluation is carried out over NC' couplings measured in 6 different alignment media, whereas the reported value stems from evaluation against the RDC data (NC', NH, HC') measured in 2 alignment media which was also used to refine the structure. Hence, the much lower reported value of 11% reflects that it is not a free R-value and the different choice of couplings (NC' only vs. NC', NH, HC', C_{α} - H_{α} ,...). Here, for reasons of consistency we evaluated R for 1d3z on the same RDC data as used for all other ensembles. However, two of the six NC'-RDC data sets used here for cross-validation have already been used in Ref. [2] for the refinement of the ensemble 1d3z. The R_{free} taken for the remaining 4 NC'-RDC data sets that were not used to refine 1d3z is 29% and thus comparable to that of 1xqq. R_{free} computed in an analogous manner on 4 sets of HC'-RDC data is 23% for ensemble 1d3z (using all nonHC' RDC to fit the alignment tensor). The consistently higher Rfactors and lower correlation coefficients indicate a significant dynamic averaging effect.

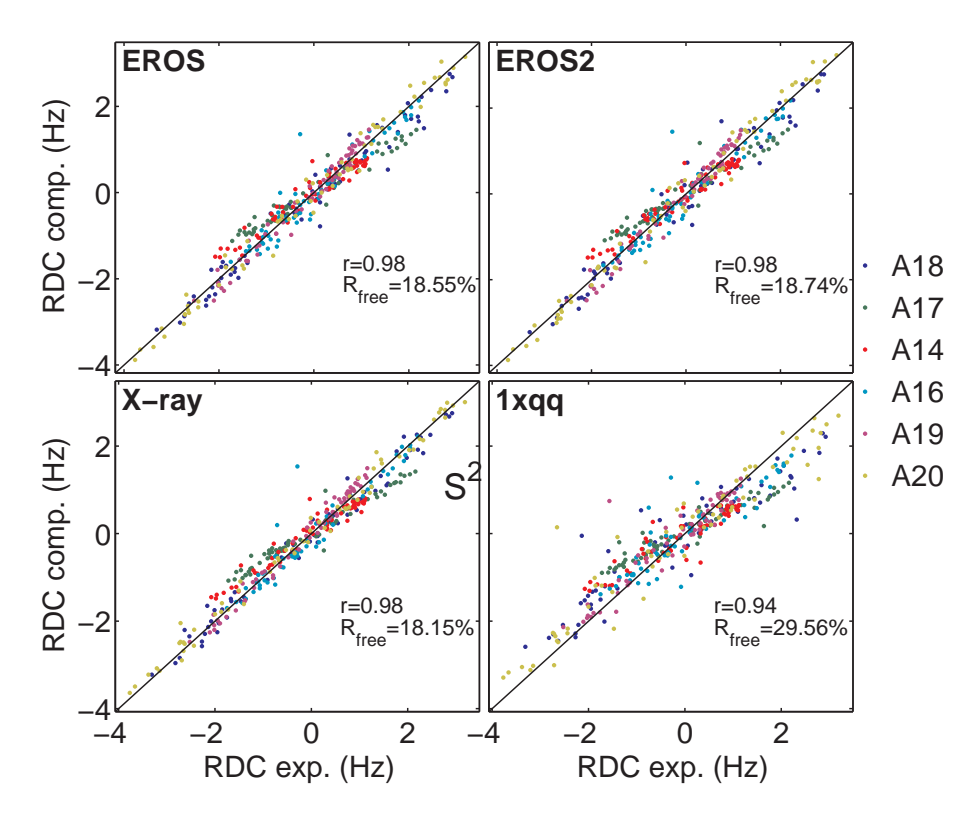


FIGURE S1. Back-calculated amide N- carbonyl C residual dipolar couplings. The colors correspond to different alignment media (cf. legend)

3.1. Scalar couplings. Scalar couplings 3J were not used in the ensemble refinement and thus are a possible candidate to further cross-validate the structural ensemble. Scalar couplings were computed using the GROMACS Software suite[4] using the parametrization of the respective Karplus curves given in 1d3z[2] for the backbone phi-dihedral and with the parametrization given in Ref. [24] (supporting information therein Table 3, Set 2) for the side-chain dihedral angles. As shown in Table S2 and Figure S2, the experimental data[24] is well reproduced by EROS ensembles. The scalar couplings were computed for each conformer and subsequently averaged. A pronounced effect of dynamical averaging on the scalar couplings can be seen for the side-chain dihedrals by considering the scalar couplings computed for the average structure of EROS (EROS_avg) or a single X-ray structure. This dynamical averaging effect is, expectedly so, much smaller for backbone dihedrals.

3.2. Scalar couplings across hydrogen bonds. Scalar couplings across hydrogen bonds $^{3h}J_{\rm NC'}$ are time averages on time-scales similar to the ones probed by RDCs[25]. Because

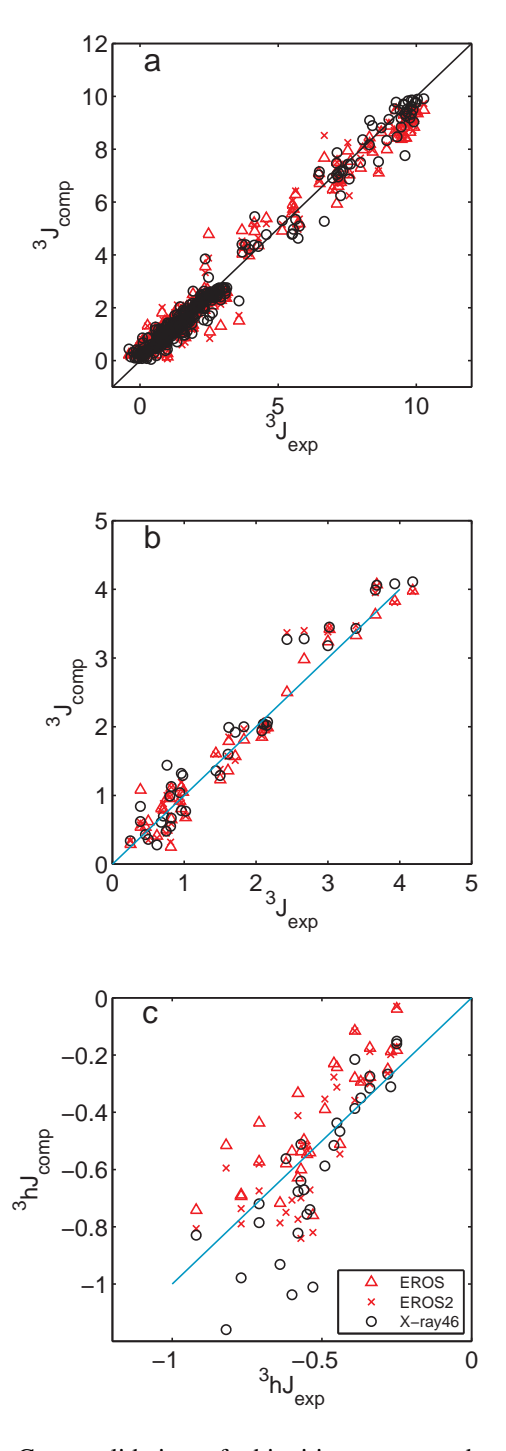


FIGURE S2. Cross-validation of ubiquitin structures by comparison with independently determined NMR data. Calculation of (a) backbone scalar couplings 3J , (b) side-chain scalar couplings, and (c) scalar couplings across hydrogen bonds $^{3h}J_{NC'}$.

of their strong dependence on H-bond geometries, they are used to cross-validate structural data[26, 17]. We have computed $^{3h}J_{\rm NC}$ for several structural ensembles using equation (6) in Ref. [27] which has been parametrized against results obtained with density functional theory. Predicted $^{3h}J_{\rm NC}$ are plotted against experimental values[28] in Fig. S2; corresponding correlation coefficients and $R_{\rm free}$, see Table S2. All ensembles show reasonable agreement, in line with previous findings[29]. As for the side-chain dihedrals χ a strong effect of dynamical averaging is observed.

4. Comparison of RDC-derived order parameters with NMR relaxation $\label{eq:data} \text{data}$

As explained in Section 1.2, relative, but not absolute order parameters of internuclear vectors can be derived from RDCs. For SCRM, therefore, RDC-based NH order parameters are shown relative to Lipari-Szabo relaxation order parameters. For EROS, absolute order parameters were derived from the RDC-refined ensemble. As the absolute dynamics is not provided by the RDCs, the overall amplitude of order parameters derived from an EROS ensemble is determined by the force field and the simulation protocol and subject to a certain uncertainty, which we estimate below. In particular, the ensemble size and the molecular mechanics force field applied will therefore determine the overall amplitude of the order parameters, whereas the relative distribution is largely determined by the RDCs (see also Section 6). We therefore investigated the role of the ensemble size and molecular mechanics force field applied in EROS on the obtained order parameters. To this end, a systematic study using a synthetic test case was carried out with ensemble sizes of 2,4, and 8 (Fig. S3). This analysis reveals that the used limited ensemble size of eight leads to an overestimation of order parameters by approximately 3%. In addition, it has been found that fast librations of NH bonds reduce the value of the RDC, which can be accounted for by using an effective NH bond length correction from 1.02 to 1.04 Å [15] and translates into an order parameter contribution of approx. 12%. Molecular dynamics simulations of lysozyme with fixed bond length suggest a uniform libration contribution of approx. 8% in the order parameters[30], which implies that this libration effect is partially, but not fully accounted for by molecular mechanics force-fields. We therefore assume that the libration contribution is underestimated in the EROS ensemble by approx. 4%. Based on this 4%

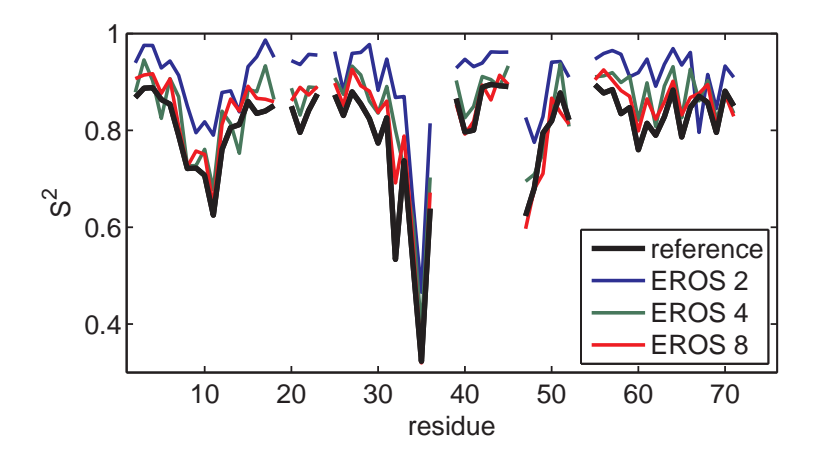


FIGURE S3. Influence of ensemble size on overall scaling of EROS order parameter. The reference shows S^2 (NH) obtained from a 168ns molecular dynamics simulation in explicit solvent. EROS was carried with ensemble sizes 2, 4 and 8 respectively. For the refinement we used 36 sets of synthetic RDCs generated from the molecular dynamics ensemble, analogous to the experimental data. The alignment tensors were obtained by fitting the trajectory against experimental data sets 1-36, couplings missing in these sets were also left out from the synthetic data set. Not shown are $S^2_{\rm EROS}$ of residues where less than 5 couplings were present in the synthetic data set. Apparently, ensemble sizes 2 and 4 underestimate the dynamics in the reference ensemble substantially. A small dampening of the dynamics of about 3% is observable for ensemble size 8.

and the above effect of limited ensemble size (3%), we thus expect that our EROS derived NH order parameters are too large by approx. 7%. To allow comparison with the Lipari-Szabo relaxation order parameters shown in Fig. 3 of the main text, the EROS order parameters were therefore scaled by 0.93. To properly reflect that this librational correction is necessarily an estimate, the resulting uncertainty in the scaling of the order parameters is depicted as a grey shaded region of $\pm 4\%$ in Fig. 3 of the main text. Note that this correction to the order parameters corresponds to a slight enhancement of the flexibility in the ensemble, leaving the conclusions about the recognition dynamics of ubiquitin unaffected.

5. Analysis of X-ray binding interfaces

Binding interfaces were analyzed for the complexes listed in Table S3. As *contacting residues* we selected all residues of a binding partner (Tab. S3, column 2) with at least one atom in less than 5 Å distance of any atom of the bound ubiquitin structure (Tab. S3, column 1). These contacting residues are shown in Figure 4a as gray spheres together with the unbound protein structure (PDB code 1UBI). Note that although some of the

contacting residues are slightly more than 5 Å away from the shown structure, they are nevertheless within 5 Å of the respective bound structure. Biologically irrelevant crystal packing contacts were ignored. Redundancies of binding interfaces, e.g., 2C7M chain A and 2C7N chain C, were removed. However, the redundancy only slightly affects the results, as seen in Figure S4, which shows the number of contacts counting also redundant interfaces.

The *number of contacts* plotted in Figure 4c was calculated by counting for every residue all atoms from the selection described above (5 Å from bound structure) that are within 10 Å of any atom of the respective residue in the unbound structure. This number count is divided by the number of atoms in the residue. The overall shape of the curve is robust against variations in the methodical details. In particular, omitting the normalization by residue size, or changing the cut-off radius from 10 Å to smaller (7 Å) or larger values (12 Å) has no significant influence on the similarity with $S_{\rm EROS}^2$.

We note that the number of contacts is affected by the chance that some binding motifs might be undiscovered so far. Moreover, contacts and $S^2_{\rm EROS}$ are very unlike observables which have no directly observable common a-priori physical basis. This renders their correlation even more notable, especially when considering that the number of 21 binding interfaces analyzed here bears already considerable statistical relevance.

5.1. Analysis of interface adaptation from solution ensemble. PCA was carried out on all (613) heavy atoms of residues 2-70 (and amide protons) after least squares fitting to backbone heavy atoms of residues 2-70 of the X-ray conformer 1UBI. The third principal component shows considerable similarity to the first principal component of the X-ray ensemble, and yields a relatively high correlation of 0.84 for a binding interface analysis analogously to Figure 5a (main text). Nevertheless, an improved collective mode was obtained as that linear combination of the first five principal components that maximizes the overlap with the X-ray ensemble.

To analyze the interface adaptation dynamics along the collective solution mode, n=30 snapshots were generated at equal distances between the extremes obtained by projecting the EROS ensemble to the extracted mode. The snapshots were aligned in PYMOL with the apo ubiquitin structure (1UBI) which was also used to align the interfaces (see above). For each combination of snapshot and binding partner the number of contacts

PDB CODE	Ubiquitin	Binding Partner	# structures used	Comments
	_	_	for X-ray ensemble	
1NBF	С	В	2	crystal contacts (chain D,A) ignored
1AAR	A	В	2	polyubiquitin
1AAR	В	A	-	
1CMX	В	A	1	contacts to C ignored
1P3Q	V	R,Q	2	contacts to U ignored
1S1Q	D	C	2	
1TBE	A	В	2	polyubiquitin
1TBE	В	A	-	
1UZX	В	A	1	ignored: redundant to 1S1Q
1XD3	В	A	2	contacts to C ignored
1YD8	U	Н	2	
2AYO	В	A	1	
2C7M	В	A	1	ignored: redundant to 2C7N_A
2C7N_A	J	C	5	
2C7N_B	Н	I	1	
2D3G	A,B	P	2	ignored: redundant to 2C7N_A
2FCQ	A	В	2	
2FID	A	В	1	ignored: redundant to 2C7N_A
2FIF	A	В	3	ignored: redundant to 2C7N_A
2G45	В	A	2	
1WR6	Е	A	4	ignored: redundant to 1YD8
1WRD	В	A	1	ignored: redundant to 1YD8
10TR, 1WR1	-	-		ignored NMR structures
1YIW			3	ignored: unbound ubiquitin
1UBI			1	
1UBQ			1	
1F9J	В	A	2	

TABLE S3. PDB codes and Chain IDs of crystallographic data used for contact analysis.

T with $3 \, \text{Å} < d < 8 \, \text{Å}$ (with d the contact distance) was counted to yield a quasi-energy E = -T. For each binding partner the snapshot with the lowest quasi-energy was selected. The x-values in Figure 5a were obtained by projecting the respective X-ray structures of ubiquitin to the collective solution mode. The "predicted" value plotted on the y-axis was obtained by interpolating between the minimal and maximal values found for the complex structure, namely $-1.71 \, \mathrm{nm}$ and $+1.13 \, \mathrm{nm}$, respectively. Then, according to the selected snapshot i, the y value was calculated as $y = -1.71 + (i-1) \left(1.13 + 1.71\right) / n$, where i, is the running number of the snapshot that has the minimal "quasi" contact-energy for the respective binding partner.

Summary of modes that were analyzed in this manner:

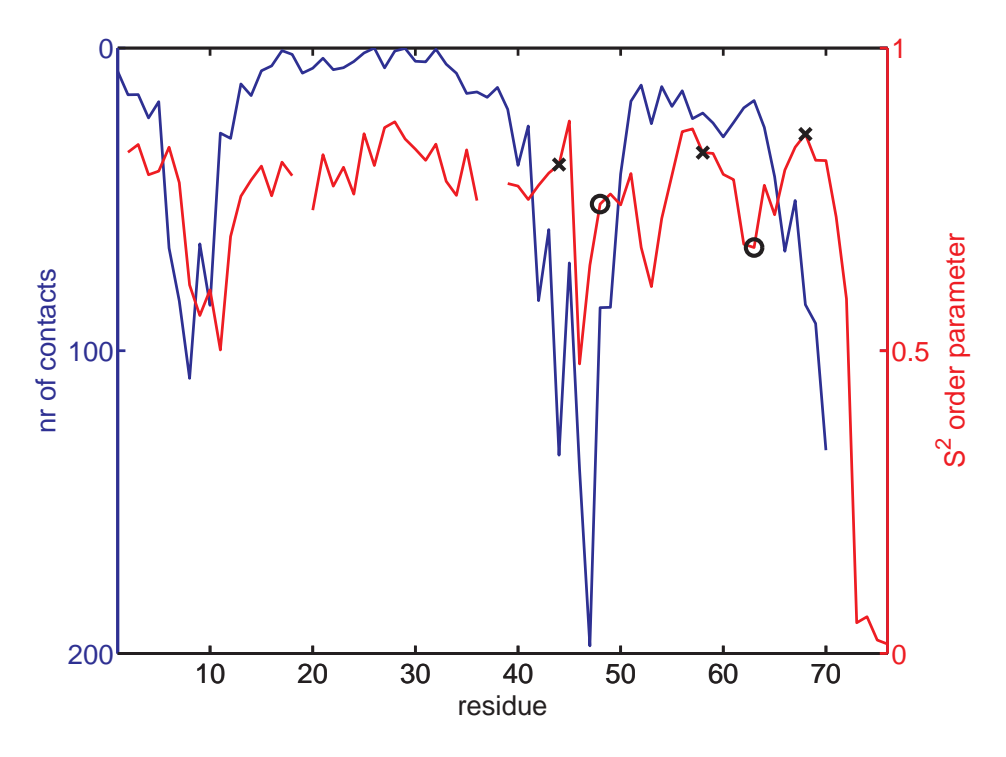


FIGURE S4. This figure shows the same analysis as Figure 4c in the main text but this time considering all (including redundant) ubiquitin complexes. Ubiquitin-binding protein contacts per residue (blue) in comparison to the flexibility in solution (red). Residues known to be crucial for molecular recognition are marked with crosses (ILE44/HIS68, ASP58). Lysines responsible for polyubiquitination are marked with circles (LYS48, LYS63).

mode3 of EROS: 0.84

linear combination of 5 PCA modes of EROS: 0.94

linear combination of 3 PCA modes of EROS: 0.9

linear combination of 5 PCA modes of EROS2: 0.85

linear combination of 5 PCA modes of 2nr2: 0.55

linear combination of 5 PCA modes of 1xqq: 0.64

6. VALIDATION OF EROS APPROACH

Cross-validation shows that the EROS ensembles agree favorably with the available experimental data. For further validation of our approach we tested the robustness of the generalized order parameters $S^2_{\rm EROS}$ (NH) of the ensembles and main principal modes obtained with principal component analysis (PCA), because these are the important observables on which our conclusions drawn in the main text rest. In particular, we systematically

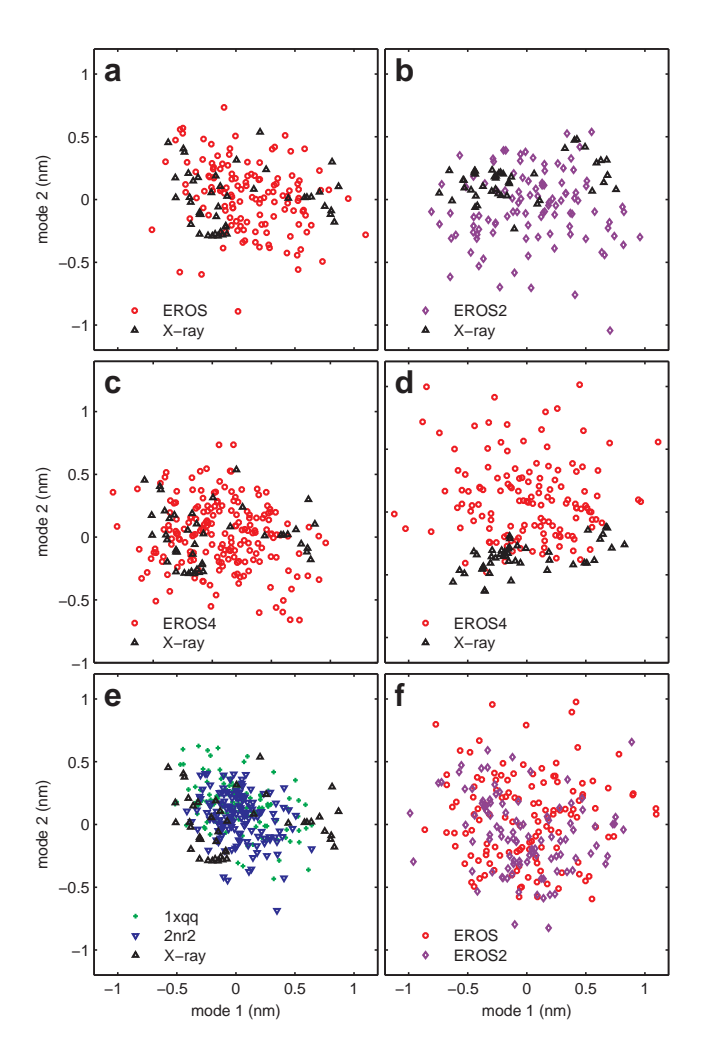


FIGURE S5. Structural comparison of ubiquitin ensembles EROS, EROS2, EROS4, 1xqq, 2nr2, and X-ray. (a,c,e) Projection of ensembles onto the principal modes that describe the interface-adaptation motion manifested in X-ray structures. (b,d,f) Direct check for systematic structural differences on the order of the overall ensemble size by carrying out PCA on pairs of ensembles that haven't been already shown in Fig. 2 of the main text. For each shown pair of ensembles (cf. legends) the principal components were extracted from the respective ensemble pairs. Note that this is different from panels (a,c,e), where the PCA was carried out over the collection of X-ray conformers, explaining the same appearance of projections of Xray structures in all three panels (a,c,e).

investigated the influence of 1) starting structure, 2) choice of force-fields, and 3) selection of RDC-data (NH only, all non NC) on our results. In the following we consider only those S^2 for which data are presented in Figure 3 of the main text. These are the residues for which model-free results were available (cf. Methods).

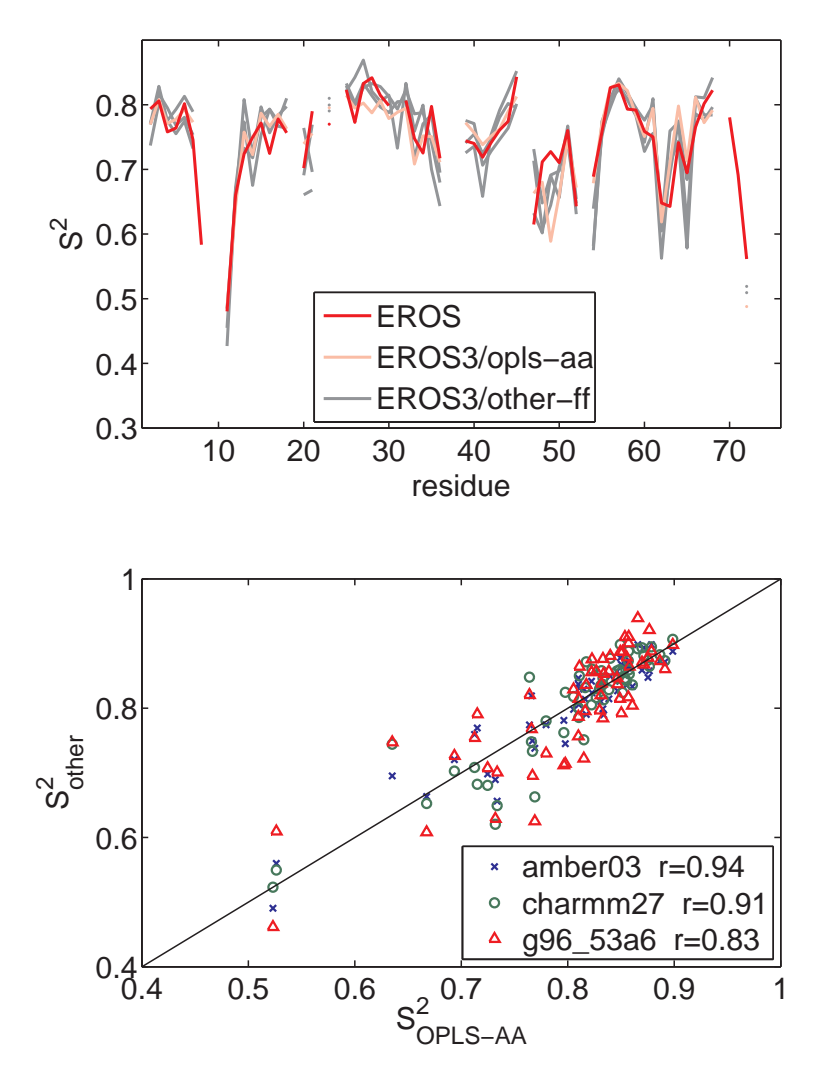


FIGURE S6. Influence of molecular dynamics force-field on NH order parameters. Upper panel: comparison of ensembles that were refined against NH RDC data sets B1-B11 and A1-A30 with different molecular mechanics force-fields. (gray: amber03, charmm27, g96_53a6; pink: opls-aa). For comparison, the order parameters $S_{\rm EROS}^2$ presented in Fig. 3 of the main text (opls-aa, experiments A1-A36) are shown in red. Lower panel: scatter plot of order parameters derived using the amber03, charmm27, and g96_53a6 force-fields compared to the opls-aa force field.

6.1. Completeness of sampling and overall scaling. To systematically assess the effect of possibly insufficient sampling in the molecular dynamics refinement step of our protocol, we started refinement from two drastically different situations. EROS refinement was started from a broad pool of structures that were obtained by CONCOORD NOE refinement from extended conformations without ever being individually refined against RDCs

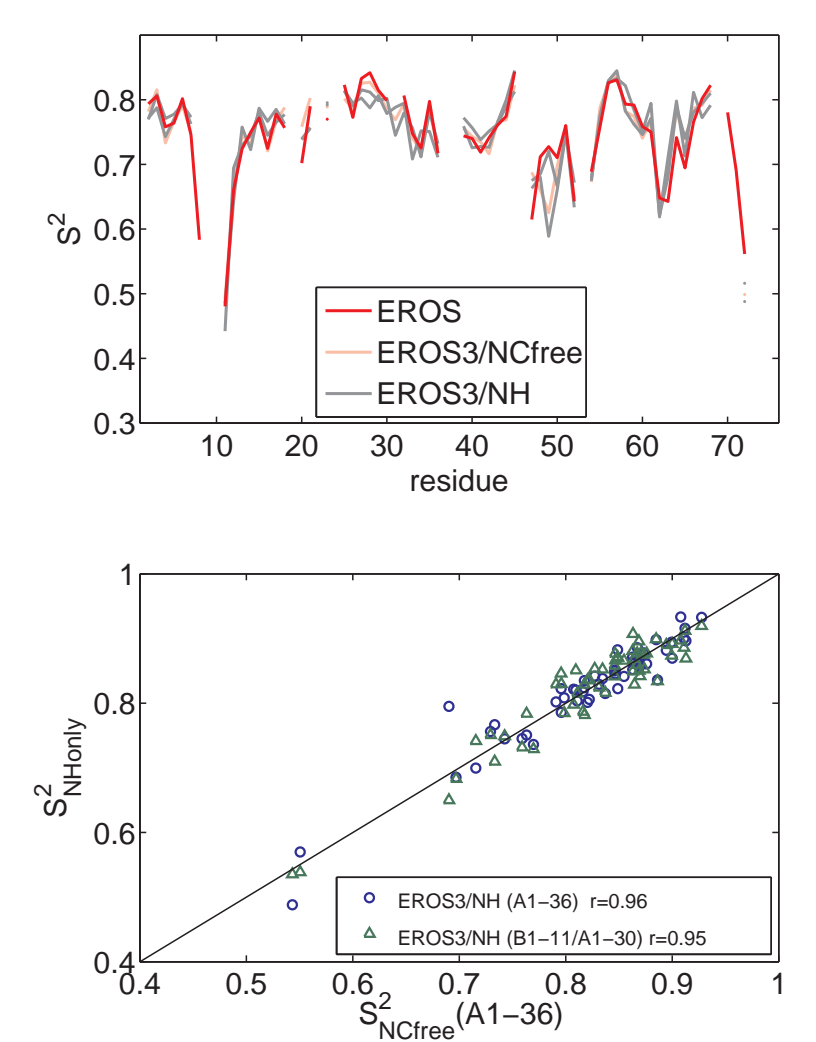


FIGURE S7. Influence of the choice of RDC data on NH order parameter S^2 . Upper panel: NH order parameters obtained from refinement carried out against residual dipolar couplings of either solely amide NH (denoted NH; gray curves) or all available couplings, but leaving N-C RDCs for cross-validation (denoted NCfree; pink/red curve). Either alignment media A1-A36 were used (pink/red/gray), or alignment media B1-B11 und A1-A30 (gray). For comparison the order parameters $S_{\rm EROS}^2$ presented in Fig. 3 of the main text (NCfree; A1-A36) are shown in red. These differ from the pink curve in terms of starting structures (see text). Lower panel: scatter plot of NH order parameters obtained from NH-only refinement against datasets B1-B11/A1-A30 and A1-A36 compared to the NCfree refinement against datasets A1-A36.

or NOEs (cf. Section S1). Thus, this pool contained considerable structural diversity (cf. Figure S9). In contrast, EROS2 refinement started from a single structure (cf. Section 1). Despite these radically different starting conditions the resulting ensembles both occupy the same region in the PCA projection shown in Fig. S9. Moreover, for both ensembles

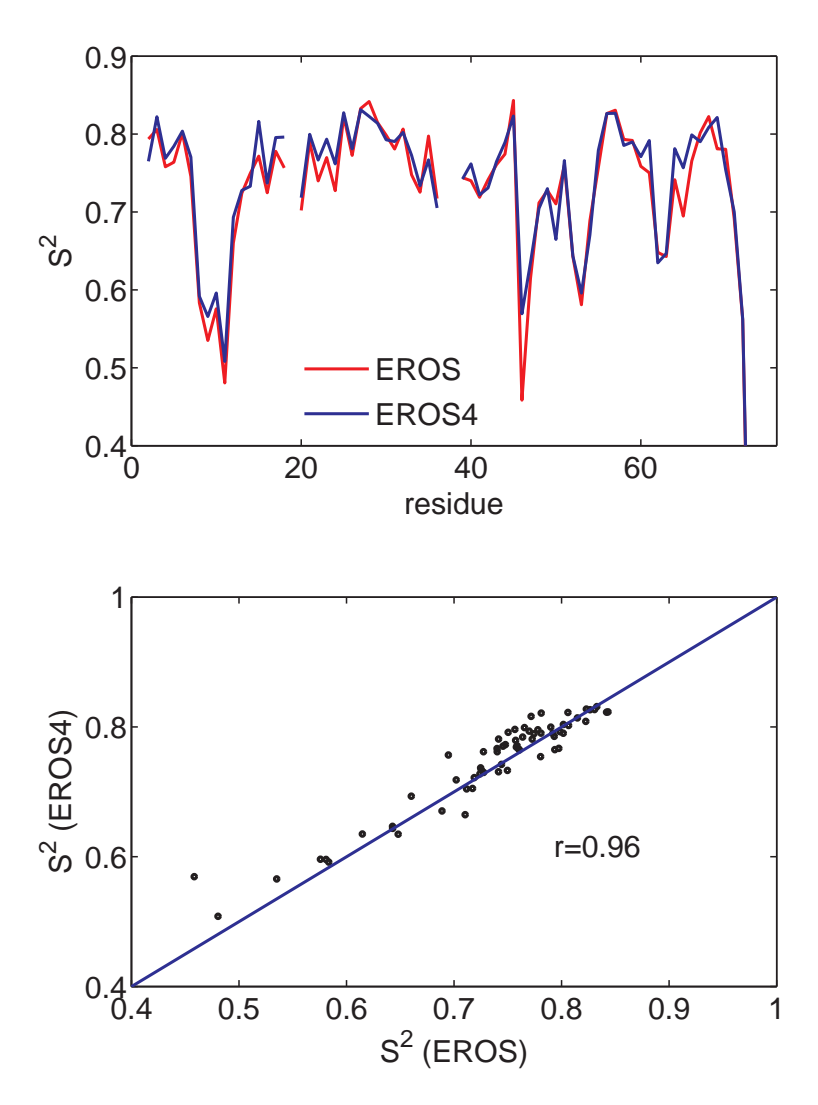


FIGURE S8. Influence of the choice of NOE data on NH order parameter S^2 . Upper panel: NH order parameters obtained from ensemble refinement carried out against residual dipolar couplings in the presence of NOE data as additional restraints (EROS) is compared to NH order parameters obtained without NOE data in the ensemble refinement (EROS4, cf. Methods). Lower panel: scatter plot of order parameters of EROS and EROS4.

the PCA shows a complete coverage of all X-ray structures (cf. Figure S5b, S5e), even the conservative EROS2 ensemble that originated from one single conformer. Finally, as can be seen in Figure S5f, EROS2 and EROS overlap strongly in the PCA projection and hence show no major systematic structural differences. Accordingly, both ensembles are indistinguishable by cross-validation (cf. Section 3).

Figure S9 shows that the RDCs have a remarkably specific effect on the structural ensembles. Starting from ensembles taken from the broad initial pool (gray), EROS sampling

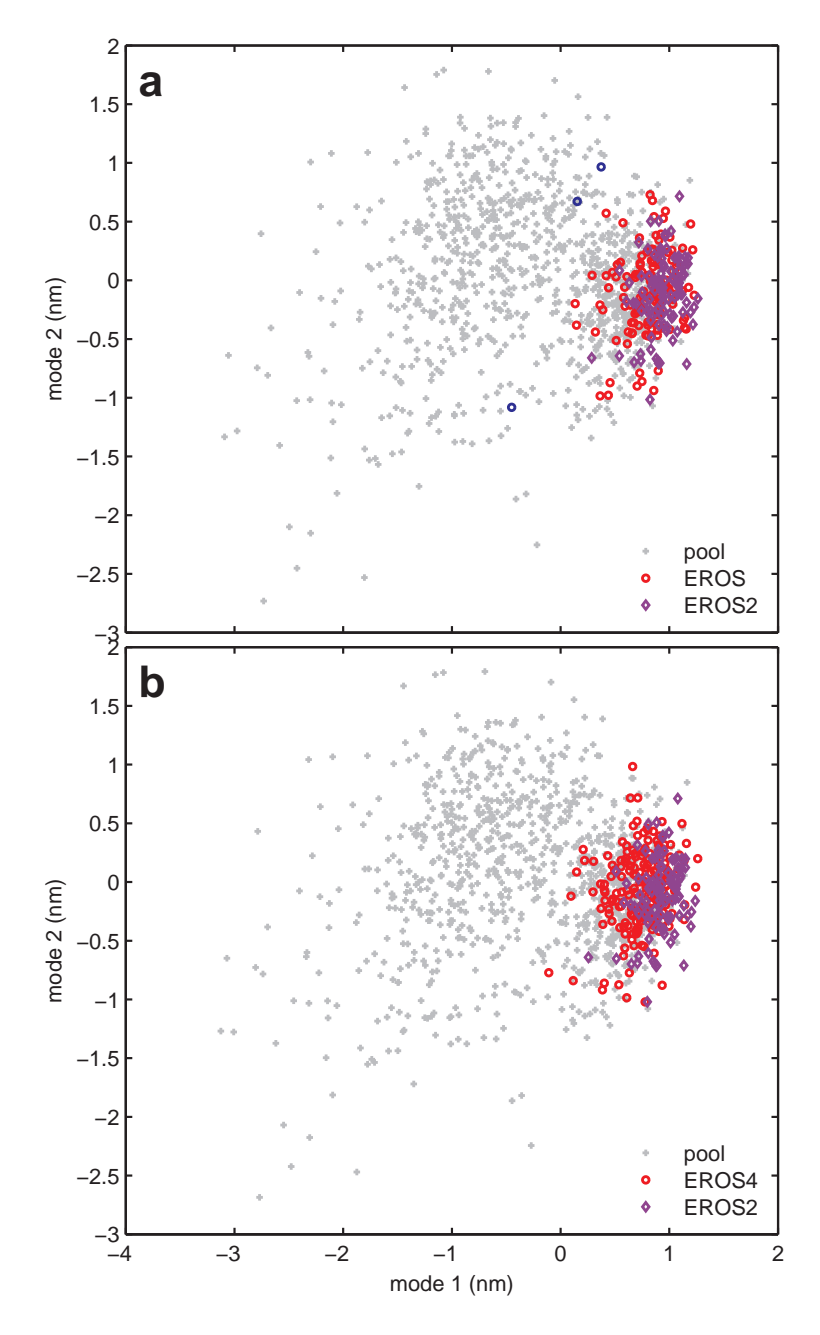


FIGURE S9. PCA projection plot to illustrate the convergence process of EROS ensemble refinement. The starting pool (gray) consists of structural pairs of ubiquitin that fulfill all NOE restraints (generated by CONCOORD, see Methods). The final EROS ensembles are shown in red and purple, respectively. The blue dots in (a) mark three structures that have been manually removed from the EROS ensemble (see text).

under the influence of the RDCs leads to a consistent drift towards the region at the right side of Figure S9 (colored circles) which is also sampled by EROS2 (diamonds). The same result is obtained for the EROS4 refinement that in contrast to the EROS refinement does not apply any NOE restraints in addition to the RDCs. This finding shows that the restraints obtained from the RDCs are sufficient to overcome sampling barriers in most instances and, therefore, the ensemble is well defined up to the remaining small differences in the overall amplitude between EROS/EROS4 and EROS2.

Three structures of the nascent EROS ensemble (Figure S9, blue circles) lie still significantly outside the region that is sampled consistently by EROS, EROS2 and EROS4, i.e., the region sampled independently of the starting conditions. Although the pool has two densely populated regions, all but these three EROS structures are found only within the region on the right side. It seems that a strong energetic barrier separates the two pool regions. Nevertheless, the pull of the RDCs is sufficient to move all but three structures into the region on the right side. Since the three outliers are found exactly at the edge of the region on the left, we concluded that for these three structures frustrated sampling may have occurred due to this barrier and, thus, a significant bias of the starting conditions may remain. Accordingly, these three structures were removed from the final EROS ensemble.

That the EROS refinement is independent from the chosen starting conditions is also supported by a comparison of order parameters $S_{\rm NH}^2$ of EROS and EROS2. Indeed, the correlation between the two sets of order parameters is high (r=0.9) confirming that both ensembles describe the same NH dynamics. The slightly smaller spread of the EROS2 ensemble revealed by PCA is reflected in a 5% increased overall amplitude of the order parameters. Note that the EROS2 ensemble suffers from limited sampling, as refinement started from a single configuration. It therefore can be considered a minimal representation of the dynamics required to fulfil the RDCs. Hence, despite that the overall amplitude of the dynamics is not directly provided by the RDCs, as discussed in section 1.3, the fact that the EROS2 ensemble shows a complete coverage of the X-ray conformers, confirms that the conclusions about the molecular recognition dynamics of ubiquitin are independent of the overall amplitude.

- 6.2. Influence of molecular mechanics force-fields. EROS ensembles have been refined against the RDCs using the state of the art all-atom force-field OPLS-AA. Here we addressed whether the dynamics as reflected by S^2 are sensitive to the applied force-field. Refinement of EROS3 was carried out with the force-fields OPLS-AA/L, AMBER03, Charmm27 and GROMOS96_53A6 (cf. Methods). As seen in Fig. S6, of EROS3 ensembles (pink and gray curves) yield order parameters similar to EROS (red curve). Moreover, correlation coefficients between order parameters derived from ensembles from the different force fields are on average r=0.9, with a slightly lower correspondence to the G96_53A6-EROS3 (r=0.83 to OPLSAA-EROS3). Hence the choice of the molecular dynamics force-field does not strongly affect the ensemble, supporting our previous conclusion that the ensembles are strongly determined by the RDC data.
- 6.3. **Selection of RDC data for refinement.** Whether our results depend on the choice of RDC data was tested by carrying out refinement with two different collections of data sets. In total, there were 47 data sets available to us for ubiquitin. The 36 data sets used throughout this work are denoted A1-A36. 11 of these data sets replace the oldest available data sets denoted B1-B11 that were obtained with much less concentrated samples than the newer sets. A control data set was constructed by selecting experiments A1-A30 and B1-B11, i.e., it was lacking the most recently acquired data sets A31-A36.

As seen in Figure S7, the change to the more recent data set has no significant effect on the $S^2_{\rm EROS}$. Moreover, Figure S7b shows that using only NH RDCs instead of all RDCs (except N-C, cf. cross-validation) has no significant effect on the $S^2_{\rm EROS}$ (NH). The ensemble refined against all non-NC work RDCs (EROS/EROS2) has a significant lower (NC) $R_{\rm free}$ value as compared to the case when only NH RDC's are used in refinement. Accordingly, this strategy was used for the ensemble presented in the main text.

7. EXPERIMENTAL DATA

7.1. Experimental data used for refinement of EROS ensembles. In this section we summarize the used RDCs: In total 47 RDC data sets have been extracted from the literature or measured in our lab. 11 of these data sets were obtained with much less concentrated samples than newer sets, and thus not used for our final refinement. The remaining 36 data sets were labelled A1-A36 (see Table S4). Since the older data the was used for EROS method validation (see Section 6), we list them here with labels B1-B11 (see Table S4).

For some of the 36 alignment conditions also other residual dipolar couplings than the amide NH were measured. A summary of these are given in Table S5 for backbone couplings and in Table S8 for methyl sidechains. The individual non-NH backbone couplings for A14, A15, A17 and A18 are given in Tables S6-S7. non-NH couplings for A19 and A20 are published elsewhere[15]. The NH couplings that are newly measured are given in the supporting information of Ref. [22]. Excluded from refinement were the 373 NC' RDCs obtained in the 6 alignment media A14, A15, and A17-20. These NC' RDCs were used for cross-validation.

Additionally, 2727 H-H NOE restraints from the data set 1d3z[2] were used.

- 7.2. **HC' and NC' RDCs.** Alignment media have been prepared as described in Ref. [22]; the nomenclature is the same as used in that manuscript. Couplings have been measured using a pulse sequence similar to Ref. [35]. In addition, two further RDC data sets from the literature have been used[15] (cf. Table S5).
- 7.3. **Side-chain methyl group RDCs.** Methyl group RDCs have been measured using the method described in Ref. [36]. Nomenclature and sample preparation was the same as described in Ref. [22]. The measured RDCs have been scaled to the CC axis along the symmetry axis: RDC(CH3 (axial)) = 0.3155 * RDC(CH3)[37]. Additionally to the side-chain methyl data measured here, we used methyl data corresponding to alignment condition A20 as published here[37].

REFERENCES

- [1] B. L. de Groot, et al., Proteins 29, 240 (1997).
- [2] G. Cornilescu, J. L. Marquardt, M. Ottiger, A. Bax, J. Am. Chem. Soc. 120, 6836 (1998).
- [3] B. Hess, R. M. Scheek, J. Mag. Res. 164, 19 (2003).
- [4] D. V. der Spoel, et al., J. Comput. Chem. 26, 1701 (2005).
- [5] U. Essmann, et al., J. Chem. Phys. 103, 8577 (1995).
- [6] T. Darden, D. York, L. Pedersen, J. Chem. Phys. 98, 10089 (1993).
- [7] W. L. Jorgensen, D. S. Maxwell, J. Tirado-Rives, J. Am. Chem. Soc. 118, 11225 (1996).
- [8] H. J. C. Berendsen, J. P. M. Postma, W. F. van Gunsteren, J. Hermans, *Intermolecular Forces*, B. Pullman, ed. (D. Reidel Publishing Company, Dordrecht, 1981), pp. 331–342.
- [9] A. D. MacKerell, et al., J. Phys. Chem. B 102, 3586 (1998).
- [10] Y. Duan, et al., J. Comput. Chem. 24, 1999 (2003).
- [11] E. J. Sorin, V. S. Pande, Biophys. J. 88, 2472 (2005).

- [12] C. Oostenbrink, A. Villa, A. E. Mark, W. F. V. Gunsteren, J. Comput. Chem. 25, 1656 (2004).
- [13] W. L. Jorgensen, J. Chandrasekhar, J. D. Madura, R. W. Impey, M. L. Klein, J. Chem. Phys. 79, 926 (1983).
- [14] B. Hess, H. Bekker, H. J. C. Berendsen, J. G. E. M. Fraaije, J. Comput. Chem. 18, 1463 (1997).
- [15] M. Ottiger, A. Bax, J. Am. Chem. Soc. 120, 12334 (1998).
- [16] A. M. J. J. Bonvin, A. T. Brunger, J. Mol. Biol. 250, 80 (1995).
- [17] B. Richter, J. Gsponer, P. Varnai, X. Salvatella, M. Vendruscolo, J. Biomol. NMR 37, 117 (2007).
- [18] J. Meiler, J. J. Prompers, W. Peti, C. Griesinger, R. Bruschweiler, J. Am. Chem. Soc. 123, 6098 (2001).
- [19] N. A. Lakomek, et al., Angew. Chem.-Int. Ed. 44, 7776 (2005).
- [20] N. A. Lakomek, T. Carlomagno, S. Becker, C. Griesinger, J. Meiler, J. Biomol. NMR 34, 101 (2006).
- [21] J. W. J. Kerssemakers, et al., Nature 442, 709 (2006).
- [22] N. A. Lakomek, et al., J. Biomol. NMR. DOI: 10.1007/s10858-008-9244-4 (2008).
- [23] G. Vriend, J. Mol. Graph. 8, 52 (1990).
- [24] J. J. Chou, D. A. Case, A. Bax, J. Am. Chem. Soc. 125, 8959 (2003).
- [25] S. Grzesiek, F. Cordier, A. J. Dingley (2001), vol. 338 of Methods in Enzymology, pp. 111–133.
- [26] G. Bouvignies, et al., Proc. Natl. Acad. Sci. U. S. A. 102, 13885 (2005).
- [27] M. Barfield, A. J. Dingley, J. Feigon, S. Grzesiek, J. Am. Chem. Soc. 123, 4014 (2001).
- [28] F. Cordier, S. Grzesiek, J. Am. Chem. Soc. 121, 1601 (1999).
- [29] H. J. Sass, F. F. F. Schmid, S. Grzesiek, J. Am. Chem. Soc. 129, 5898 (2007).
- [30] M. Buck, M. Karplus, J. Am. Chem. Soc. 121, 9645 (1999).
- [31] J. R. Tolman, J. Am. Chem. Soc. 124, 12020 (2002).
- [32] K. Ruan, J. R. Tolman, J. Am. Chem. Soc. 127, 15032 (2005).
- [33] W. Peti, J. Meiler, R. Bruschweiler, C. Griesinger, J. Am. Chem. Soc. 124, 5822 (2002).
- [34] H.-J. Sass, G. Musco, S. J. Stahl, P. T. Wingfield, S. Grzesiek, J. Biomol. NMR 18, 303 (2000).
- [35] K. Ding, A. M. Gronenborn, J. Mag. Res. 158, 173 (2002).
- [36] G. Kontaxis, A. Bax, J. Biomol. NMR 20, 77 (2001).
- [37] M. Ottiger, A. Bax, J. Am. Chem. Soc. 121, 4690 (1999).

Source	code	NH
SCRM 2008[22]	A1	60
SCRM 2008	A2	59
SCRM 2008	A3	56
SCRM 2008	A4	62
SCRM 2008	A5	48
SCRM 2008	A6	53
SCRM 2008	A7	62
SCRM 2008	A8	61
SCRM 2008	A9	56
SCRM 2008	A10	61
SCRM 2008	A11	59
SCRM 2008	A12	61
SCRM 2008	A13	59
Lakomek et al. 2006[20]	A14	51
Lakomek et al. 2006	A15	48
Lakomek et al. 2006	A16	53
Lakomek et al. 2006	A17	47
Lakomek et al. 2006	A18	44
Ottiger et al.[15]	A19	63
Ottiger et al.	A20	60
Tolman 2002[31]	A21	44
Tolman 2002	A22	46
Tolman 2002	A23	46
Tolman 2002	A24	45
Tolman 2002	A25	47
Tolman 2002	A26	44
Tolman 2002	A27	48
Tolman 2002	A28	44
Tolman 2002	A29	54
Ruan & Tolman 2005[32]	A30	43
Ruan & Tolman 2005	A31	37
Ruan & Tolman 2005	A32	48
Ruan & Tolman 2005	A33	51
Ruan & Tolman 2005	A34	50
Ruan & Tolman 2005	A35	56
Ruan & Tolman 2005	A36	61

Source	code	NH
Peti et al. 2002[33]	B1	61
Peti et al. 2002	B2	58
Peti et al. 2002	В3	52
Peti et al. 2002	B4	57
Peti et al. 2002	B5	67
Lakomek et al. 2006[20]	В6	59
Lakomek et al. 2006	B7	59
Lakomek et al. 2006	B8	51
Lakomek et al. 2006	B9	63
Lakomek et al. 2006	B10	35
Sass et al. 2000[34]	B11	56

TABLE S4. Experimental sources of NH RDCs used for EROS refinement and SCRM. The second column lists the code assigned to each experimental condition. The last column shows the number of couplings obtained for the amide NH intereaction in the respective alignment medium.

Source	code	NC'	HC'	C_{α} C'	$C_{\alpha}H_{\alpha}$	$C_{\alpha}C_{\beta}$
Ottiger et al.[15]	A19	61	61	58	62	39
Ottiger et al.	A20	63	63	54	62	
Lakomek et al. 2006[20]	A14	63	60			
Lakomek et al. 2006	A15	64	64			
Lakomek et al. 2006	A17	63	64			
Lakomek et al. 2006	A18	59	61			

TABLE S5. Experimental sources of the non-NH backbone residual dipolar couplings used for EROS refinement. The second column lists the code assigned to each experimental conditions. The last five columns show the numbers of couplings obtained for the respective types of heteronuclear coupling vectors.

NC'	A14	A15	A17	A18
	E1	E3	E4	E5
1	-2,21	-1,75	0,65	0,06
2	3,31	1,36	-0,91	0,58
3	-2,05	-1,33	1,98	-2,05
4	1,46	0,71	-1,10	0,29
5	-1,92	-0,88	1,66	-2,21
6	0,41	0,63	-1,06	0,34
7	2,27	1,30	-0,75	n
8	n	n	n	n
9	1,59	0,88	-0,33	0,75
10	-1,98	-1,53	0,55	-0,81
11	2,27	1,27	-0,41	n
12	-1,10	-0,65	0,03	0,75
13	n	0,55	0,86	-1,23
14	-0,13	0,58	-0,97	0,97
15	-2,79	-1,85	2,08	-1,88
16	-0,45	0,49	-0,89	-0,10
17	-0,75	-0,10	-0,13	1,43
18	n	n	n	n
19	-2,92	-2,16	1,82	-1,95
20	-0,36	n	n	1,07
21	1,67	0,47	-0,89	0,96
22	-0,03	0,23	1,17	-1,69
23	n	n	n	n
24	2,73	1,27	-0,33	0,10
25	-2,86	-1,85	1,20	-2,05
26	2,21	1,72	-0,81	0,91
27	2,21 n	n	1,51	n
28	1,85	0,49	-0,86	0,42
29	-1,01	-0,16	1,12	-1,92
30	-0,55	-0,75	-0,33	1,10
31	1,95	0,71	0,29	-0,45
32	-2,27	-1,72	0,81	-1,49
33	0,91	1,36	-0,03	-0,26
34	-2,32	-1,64	0,67	0,08
35	-1,44	-0,31	-0,31	-1,25

Table S6: NC' experimental residual dipolar couplings for the alignment media A14, A15, A17, and A18 that have been newly measured for the presented analysis. The second row contains the corresponding nomenclature for the alignment media as used in Lakomek et al. 2006

NC'	A14	A15	A17	A18
36	n	n	n	n
37	n	n	n	n
38	2,63	0,97	-1,10	1,01
39				
40	2,08	0,88	-0,03	n
41	-2,47	-2,05	1,46	-1,17
42	1,66	0,65	-0,33	0,29
43	-1,33	-1,36	0,33	0,39
44	0,37	0,57	-1,12	0,21
45	-0,75	-0,29	0,78	n
46	2,14	0,91	-1,04	0,58
47	-1,77	-1,45		
48	1,92	0,84	-1,07	1,07
49	-1,59	0,10	0,68	-1,59
50	-0,94	-0,42	0,10	0,78
51	0,03	-0,49	-0,62	-0,29
52	n	n	n	n
53	-2,19	-1,93	0,89	-0,44
54	2,82	1,23	-0,91	0,62
55	0,26	1,56	-0,88	1,14
56	-0,13	-0,42	0,81	0,71
57	2,53	1,07	-0,97	1,36
58	-0,29	0,34	-0,84	1,20
59	2,01	0,81	0,44	-0,32
60	-1,07	-0,52	-0,33	-1,07
61	-0,06	-0,29	-0,42	1,10
62	1,95	1,59	0,08	n
63				
64	,			1,75
65			1,56	
66	-0,55			
67	1,75	1,43	0,16	-0,16
68	0,52	-0,26	0,03	
69	1,40	1,46	-1,09	1,36
70	2,16	1,25	-0,46	
71	-1,56	-1,17	0,39	0,36

HC'	A14	A15	A17	A18
(2006)	E1	E3	E4	E5
		n	n	n
2	2,48	2,73	0,48	-1,04
3			2,57	
4				
5	n	-0,72		
6	5,21			
7	1,04			-2,00
8				
9	n	n	n	n
10	-0,72	-0,96	2,16	-2,32
11	0,80	1,12	0,96	-1,12
12	-4,17	-3,73	0,40	-0,96
13		-0,80	1,68	
14	3,01	-1,00	-0,84	3,17
15	0,72			0,08
16	7,93	4,81		
17	0,40	0,40	1,36	
18	-0,96	-0,40	0,88	-3,37
19		n	n	n
20	4,97	2,57	-3,21	5,77
21				
22	2,97	1,76	0,12	1,04
23	n	-1,36		
24	n	n	n	n
25	-5,61	-2,00	2,16	-1,12
26	5,53	1,04		4,09
27	-2,89	-3,13	1,44	-2,72
28	-2,89 2,24	-3,13 1,52	1,44 -1,04	-2,72 -0,64
29	-2,40	-0,56	2,20	0,16
30	2,48	-1,12 0,48	-0,16 0,72	2,16
31	0,32	0,48	0,72	-3,53
32	-4,49	-1,52	0,56	-0,96
33	4,65	1,92	0,00	3,53
34		-2,65	1,44	
35		3,45		0,96
36	-1,36	0,32	1,20	0,56

Table S7: HC' experimental residual dipolar couplings for alignment conditions A14, A15, A17, and A18 that have been newly measured for the presented analysis.

HC'	A14	A15	A17	A18
37	n	n	Ν	n
38	n	n	Ν	n
39	-1,52	0,72	1,36	0,08
40	n	-2,61		
41	1,76		-1,84	
42	5,77	4,25	-2,48	n
43	-0,24	0,24	0,16	-1,84
44	2,08			-2,72
45	1,20	-1,76	1,12	-1,68
46	n	n	Ν	n
47	-2,16	-1,48	2,73	-1,68
48				
49	-5,57	-3,41		
50	2,08	-1,60	0,48	0,16
51	-0,68			-1,32
52	-7,13	-1,68		
53	n	n	Ν	n
54	4,49	3,69	-2,57	0,64
55	-4,17	-1,60	1,52	-0,64
56	1,84	-1,76	0,24	0,88
57	4,57	3,37	-3,77	3,45
58	-2,32			-0,88
59	0,80	-2,00	2,00	-0,80
60	0,32	1,52	-1,76	
61	4,41	3,29	-1,20	
62	4,65	3,29	-2,08	0,16
63	-6,73	-2,48	-0,24	0,96
64	n	n	1,44	1,68
65	2,89	.,	0,08	-2,40
66	6,01	2,52	-3,69	6,01
67	4,49	2,16	-0,64	3,69
68	-1,68		1,20	
69	2,40	0,48		
70	0,24	-0,96		
71	-0,96	0,24		

methyl		Spin1	Spin2	A1	A2	А3	A4	A7	A8	A9	A10	A12	A13
AA	Res												
MET	1	SD	CE	n	n	n	n	N	n	n	n	n	n
ILE	3	CG1	CD1	0,61	0,80	2,46	-1,40	-1,10	-0,55	1,06	-0,20	-0,98	-1,87
ILE	3	СВ	CG2	0,90	1,43	2,54	n	-1,13	-1,34	-4,24	-0,81	-1,76	-2,36
VAL	5	СВ	CG1	n	n	n	n	N	n	n	n	n	n
VAL	5	СВ	CG2	-0,16	-0,15	-0,70	1,49	0,65	-0,21	-2,01	-0,04	0,14	0,95
THR	7	СВ	CG2	-0,77	-0,86	-5,62	1,35	0,90	1,06	-0,18	0,09	0,84	1,89
LEU	8	CG	CD1	0,53	0,66	1,22	-1,01	-1,20	-0,67	-1,08	-0,73	-1,44	-1,95
LEU	8	CG	CD2	n	n	n	n	N	n	n	n	n	n
THR	9	СВ	CG2	0,57	1,05	2,25	-2,36	-3,17	-1,28	-2,60	-1,79	-3,64	-3,94
THR	12	СВ	CG2	0,37	1,19	1,54	0,14	-1,09	-1,22	-4,59	-0,82	-1,84	-1,90
ILE	13	CG1	CD1	-0,01	-0,05	1,42	-1,20	-0,55	-0,17	1,24	-0,25	-0,64	-0,79
ILE	13	СВ	CG2	-0,72	-0,95	-2,76	1,40	1,43	0,86	0,23	0,53	1,31	2,30
THR	14	СВ	CG2	0,42	1,29	1,14	-0,53	-2,21	-1,24	-4,99	-1,52	-2,96	-3,35
LEU	15	CG	CD1	n	n	n	n	n	n	n	n	n	n
LEU	15	CG	CD2	-0,13	-0,48	0,38	0,53	1,43	0,35	1,73	0,86	0,31	1,25
VAL	17	СВ	CG1	n	n	n	n	n	n	n	n	n	n
VAL	17	СВ	CG2	-1,13		-1,55	1,20	2,52	•	3,74	1,47	2,91	4,19
THR	22	СВ	CG2	-0,19	-0,24	0,11	1,68	0,94	•	-1,93	0,14	0,37	0,82
ILE	23	CG1	CD1	0,26	0,33	2,59	-1,16	-1,39	•	0,47	-0,37	-1,15	-1,54
ILE	23	СВ	CG2	0,31	1,00		-0,05	-1,66	•	-5,52	-1,45	-2,41	-2,32
VAL	26	СВ	CG1	-0,93	-1,72	-0,84	1,93	3,05	0,90	2,87	1,22	2,81	4,24
VAL	26	СВ	CG2	n	n	n	n	n	n	n	n	n	n
ALA	28	CA	СВ	n	n	n	n	n	n	n	n	n	n
ILE	30	CG1	CD1	0,11	-0,48		0,48	1,75		3,13	1,27	2,14	1,93
ILE	30	СВ	CG2	0,04	0,43		0,38	-1,51	-0,69	-4,89	-1,06	-1,66	-2,47
ILE	36	CG1	CD1	-0,54	-1,00		0,34	1,25	•	1,13	0,44	0,92	1,52
ILE	36	СВ	CG2	0,53	0,81	-1,32	-1,16	-1,44	0,03	0,41	-0,33	-0,78	-1,68
LEU	43	CG	CD1	n	n	n	n	n	n	n	n	n	n
LEU	43	CG	CD2	-0,04	-0,20	1,66	0,39	1,33	0,07	2,02	0,80	1,51	1,24

Table S8: Experimental residual dipolar couplings for methyl groups, that have been newly measured for the presented analysis. Data set A20 has been taken from Ref. [36].

met	hyl	Spin1	Spin2	A7	A2	A1	А3	A4	A9	A8	A10	A13	A12	A20
AA	Res													
ILE	44	CG1	CD1	-0,11	0,28	0,10	0,01	0,10	-1,12	-0,27	-0,32	-0,32	-0,41	-0.25
ILE	44	СВ	CG2	2,57	-1,00	-0,30	-1,85	1,11	3,86	1,24	1,59	3,44	2,81	3.15
ALA	46	CA	СВ	-2,82	1,87	1,01	2,89	-1,06	-7,63	-2,42	-2,04	-4,85	-4,31	-4.56
LEU	50	CG	CD1	-1,30	0,90	0,52	-0,76	-1,11	1,03	0,21	-0,17	-1,63	-1,65	-1.52
LEU	50	CG	CD2	-0,11	0,57	0,37	2,05	0,14	-0,83	-0,52	0,37	-0,47	0,19	-0.52
THR	55	СВ	CG2	4,12	-2,19	-1,41	-2,79	2,12	4,57	1,46	1,55	5,85	4,00	5.04
LEU	56	CG	CD1	n	n	n	n	n	n	n	n	n	n	
LEU	56	CG	CD2	-0,77	0,28	-0,06	-2,48	0,05	-3,02	-0,09	-1,10	-1,04	-1,40	-0.70
ILE	61	CG1	CD1	-1,47	0,37	0,12	2,09	-1,30	-1,88	-0,88	-1,02	-2,30	-2,06	-2.24
ILE	61	СВ	CG2	1,35	0,42	0,37	2,28	0,58	2,37	-0,02	1,32	1,14	1,89	0.91
THR	66	СВ	CG2	n	n	n	n	n	n	n	n	n	n	
LEU	67	CG	CD1	-0,71	-0,20	-0,05	0,25	-1,11	-0,56	-0,19	-0,71	-0,95	-1,07	-0.80
LEU	67	CG	CD2	2,50	-1,24	-0,73	-0,61	1,16	3,01	0,94	1,33	3,19	2,44	3.12
LEU	69	CG	CD1	n	n	n	n	n	n	n	n	n	n	
LEU	69	CG	CD2	n	n	n	n	n	n	n	n	n	n	
VAL	70	СВ	CG1	n	n	n	n	n	n	n	n	n	n	
VAL	70	СВ	CG2	0,99	-0,81	-0,45	1,38	0,34	2,10	0,19	0,72	1,47	1,14	1.33
LEU	71	CG	CD1	n	n	n	n	n	n	n	n	n	n	
LEU	71	CG	CD2	0,53	0,37	0,20	0,94	0,34	-0,79	-0,45	0,20	-0,07	0,26	Ν
LEU	73	CG	CD1	1,13	-0,48	-0,19	-0,64	0,87	0,14	0,10	0,44	1,10	0,83	1.04
LEU	73	CG	CD2	0,97	-0,20	-0,10	-1,57	0,43	1,78	0,67	0,71	1,03	1,12	1.09

Table S8 (continued): Experimental residual dipolar couplings for methyl groups